

Article

Landslides Triggered by the 2016 Heavy Rainfall Event in Sanming, Fujian Province: Distribution Pattern Analysis and Spatio-Temporal Susceptibility Assessment

Siyuan Ma ^{1,2}, Xiaoyi Shao ^{3,4} and Chong Xu ^{3,4,*} ¹ Institute of Geology, China Earthquake Administration, Beijing 100029, China; masiyuan@ies.ac.cn² Key Laboratory of Seismic and Volcanic Hazards, Institute of Geology, China Earthquake Administration, Beijing 100029, China³ National Institute of Natural Hazards, Ministry of Emergency Management of China, Beijing 100085, China; xiaoyishao@ninhm.ac.cn⁴ Key Laboratory of Compound and Chained Natural Hazards Dynamics, Ministry of Emergency Management of China, Beijing 100085, China

* Correspondence: chongxu@ninhm.ac.cn or xc1111111@126.com

Abstract: Rainfall-induced landslides pose a significant threat to the lives and property of residents in the southeast mountainous area. From 5 to 10 May 2016, Sanming City in Fujian Province, China, experienced a heavy rainfall event that caused massive landslides, leading to significant loss of life and property. Using high-resolution satellite imagery, we created a detailed inventory of landslides triggered by this event, which totaled 2665 across an area of 3700 km². The majority of landslides were small-scale, shallow and elongated, with a dominant distribution in Xiaqu town. We analyzed the correlations between the landslide abundance and topographic, geological and hydro-meteorological factors. Our results indicated that the landslide abundance index is related to the gradient of the hillslope, distance from a river and total rainfall. The landslide area density, i.e., LAD increases with the increase in these influencing factors and is described by an exponential or linear relationship. Among all lithological types, Sinian mica schist and quartz schist (Sn-s) were found to be the most prone to landslides, with over 35% of landslides occurring in just 10% of the area. Overall, the lithology and rainfall characteristics primarily control the abundance of landslides, followed by topography. To gain a better understanding of the triggering conditions for shallow landslides, we conducted a physically based spatio-temporal susceptibility assessment in the landslide abundance area. Our numerical simulations, using the MAT.TRIGRS tool, show that it can accurately reproduce the temporal evolution of the instability process of landslides triggered by this event. Although rainfall before 8 May may have contributed to decreased slope stability in the study area, the short duration of heavy rainfall on 8 May is believed to be the primary triggering factor for the occurrence of massive landslides.

Keywords: landslides; heavy rainfall; distribution pattern; spatiotemporal assessment; Sanming area; Fujian province



Citation: Ma, S.; Shao, X.; Xu, C. Landslides Triggered by the 2016 Heavy Rainfall Event in Sanming, Fujian Province: Distribution Pattern Analysis and Spatio-Temporal Susceptibility Assessment. *Remote Sens.* **2023**, *15*, 2738. <https://doi.org/10.3390/rs15112738>

Academic Editors: Ioannis Papoutsis, Konstantinos G. Nikolakopoulos and Constantinos Loupasakis

Received: 6 April 2023

Revised: 22 May 2023

Accepted: 22 May 2023

Published: 24 May 2023



Copyright: © 2023 by the authors. Licensee MDPI, Basel, Switzerland. This article is an open access article distributed under the terms and conditions of the Creative Commons Attribution (CC BY) license (<https://creativecommons.org/licenses/by/4.0/>).

1. Introduction

Rainfall-induced landslides are a type of slope instability that may occur in densely distributed soil and/or debris under heavy rainfall, producing a significant amount of sediments in river networks [1,2]. These landslides often result in catastrophic debris flows, which cause severe damage to agricultural crops, infrastructure and human lives [3,4]. Therefore, effective risk mitigation measures and early warning systems are urgently needed to minimize the detrimental impacts of these slope instabilities on both local and regional scales [5–7].

The southeast coastal area of China falls within the subtropical monsoon climate zone and is frequently affected by typhoons and rainstorms. The coastal areas are characterized

by mountainous and hilly terrains, which cover approximately 75% of the total area. The climate in this region is warm and humid with abundant rainfall, leading to strong physical weathering of rocks [8]. The slope surfaces in this area are predominantly covered by residual soil and heavily weathered rocks. As a result, approximately 90% of landslides occur during the rainy seasons, which typically span from May to September. During these months, landslides triggered by heavy rainfall events are the primary cause of building damage and human casualties. In August 2005, a landslide triggered by Typhoon “Sudilo” caused direct economic losses amounting to USD 4.0 million in Zhejiang Province and posed a threat to 4616 local residents. On 10 June 2019, Longchuan County, Guangdong Province, China, was subjected to incessant heavy rainfall, which subsequently led to widespread landslides, collapses and debris flows. Among the 352 affected villages, Mibei village in Longchuan County was hit the hardest, with 1571 individuals affected, 120 buildings completely destroyed and over 100 houses sustaining damage of varying degrees. The direct economic loss of this event reached USD 15.4 million [9]. In June 2019, due to the influence of southwest airflow on the south side of low-level shear, heavy rainfall occurred in the western region of Fujian Province. Since 6 June, 75,900 people have been affected in 19 counties of Sanming, Nanping and Longyan cities, resulting in a direct economic loss of USD 37.9 million. Rainfall-induced landslides have seriously affected the life safety as well as economic development in the southeastern coastal areas. Therefore, the study of distribution characteristics and spatiotemporal prediction of such landslides has become a major demand for ensuring national security and social development.

For the analysis of regional landslides induced by a single extreme event (e.g., earthquake or heavy rainfall), a comprehensive landslide inventory is essential and often indispensable. Such data provide a crucial foundation for the distribution characteristics of landslides [10], susceptibility and risk assessment [11,12], landslide formation mechanism and geomorphological evolution [13,14]. In contrast to earthquake events, the database of landslides triggered by heavy rainfall events is still limited [15–17]. At present, only 16 public rainfall-event-based landslide databases are available worldwide, but most of these event-based databases are small in scale. There are only four landslide databases with more than 2000 landslides, including the Morakot Typhoon event in southern Taiwan on August 6–9, 2008 [18], the heavy rainfall event in the Teresópolis region of Brazil on 11–13 January [17], as well as the long-term heavy rainfall event in Japan’s Hiroshima region from 28 June to 9 July 2018 [19] and the Hurricane Maria event in Dominica region from 18–22 September 2017 [20,21]. Therefore, compared to earthquake-event-based landslide inventories, the landslide inventories associated with heavy rainfalls still need more in-depth investigations.

Assessing the spatial susceptibility of rainfall-induced landslides plays an important role in effective landslide prevention and control [22–25]. Currently, three primary methods are pervasively used for rainfall-induced landslide prediction: empirical models [26–28], data-driven models [24,29] and physically based models [30,31]. The empirical model is primarily based on the analysis of rainfall characteristics, such as rainfall intensity, duration and total amount. This type of model is utilized to determine the likelihood of landslides. Although this method is simple and easy to implement, it only considers rainfall as a single factor and ignores other important topographical, geological and hydrological factors. In addition, empirical models require abundant landslide and rainfall data to determine the empirical rainfall threshold. Due to the lack of landslide and rainfall data, it is difficult to develop an efficient rainfall threshold model in mountainous areas with severe landslide disasters [5,28]. The statistical model analyzes the relationship between various factors, such as elevation, hillslope gradient, slope aspect, average rainfall and vegetation coverage. Then, based on data-driven models and actual landslides, a rainfall-induced landslide assessment model is created [15,32]. However, this method cannot explain the physical mechanism of landslide occurrence and requires a large amount of landslide data; otherwise, because it requires sufficient landslide data to establish the susceptibility

assessment model, this results in assessment results that frequently lag behind practical application and cannot serve the emergency assessment in a short time [33].

The physically based method does not use actual landslide data but rather simulates the physical process of rainfall-induced landslide occurrence by combining hydrological and infinite slope models. Physical models can reproduce the physical process of landslide occurrence, which is considered to be an effective method for landslide susceptibility analysis [34]. Furthermore, the GIS technology has facilitated the widespread use of physically based models in large regions. As a result, physically based models have been widely used in the prediction and early warning of rainfall-induced landslides [35,36]. Currently, commonly used physical models for landslide susceptibility assessment include the SHALSTAB [37] and SINMAP models [38] based on steady-state hydrological modeling, as well as the SLIP [2,39], CRESTSLIDE [40], HIRESSES [41,42] and TRIGRS models [43] based on transient physical modeling. At present, the TRIGRS model has been widely used worldwide including in Italy, the United States, China, South Korea and Southeast Asia [9,43–46], and is currently one of the most popular models for the spatiotemporal prediction of rainfall-induced landslides. However, the application of the TRIGRS model in China's southeast area is limited, so it is necessary to investigate the applicability of the model in the southeast mountainous area.

From 5 to 10 May 2016, Sanming City in Fujian Province, China, experienced an unprecedented heavy rainfall event with a maximum hourly rainfall of 56.6 mm and a maximum daily rainfall of 259.6 mm, breaking the local daily rainfall record of 178.2 mm set in 1961. This rainfall event triggered extensive landslides, resulting in significant loss of people's lives and property. During this rainfall event, a landslide occurred in the Chitan Village of Kaishan Township, leading to the burial of the office building and construction site dormitory of the expansion project of the Chitan hydropower plant, which belongs to the China Huadian Corporation. As of 1:00 pm on 10 May, the landslide had caused 35 deaths and one person was missing. To better understand the characteristics of the landslides induced by this fatal event, a comprehensive landslide inventory is needed. Therefore, the objectives of this study are twofold: (1) to establish a rainfall-induced landslide inventory through visual interpretation and to analyze the distribution pattern of landslides with relevant factors; and (2) to achieve physically based spatiotemporal susceptibility assessments using an open-source tool of MAT.TRIGRS (V1.0) and to back-analyze the rainfall process' response to changes in landslide stability. This study can provide a significant scientific basis for the formation mechanism and spatiotemporal prediction of rainfall-induced landslides in the southeast coastal area.

2. Study Area

The study area is located in the western part of Fujian Province, between 25°30'N–27°07'N latitude and 116°22'E–118°39'E longitude. It neighbors Fuzhou to the east, connects Jiangxi Province to the west and borders Nanping to the north. The landform of the study area is mainly hilly terrain, with medium- and low-elevation mountains. Geologically, the area is an erosion-dominated mountainous region with strong tectonic activity. The terrain is generally higher in the southeast and lower in the northwest, with elevations ranging from 130 m to 1847 m (Figure 1). In addition, the area features a subtropical monsoon climate with a typical mountain climate. The rainfall is abundant, with an annual average precipitation reaching up to 1700 mm. The rainfalls are mainly concentrated from March to August and the annual average temperature is about 19.9 °C.

Figure 2 illustrates the distribution of the main lithology exposed in the study area, which ranges from Quaternary loose deposits (Q) to Proterozoic granite (Pt-g). The main lithology is protozoic plagioclase hornblende and granulite (Pt-p), which are mainly distributed in the north of the study area. In addition, Jurassic variegated sandstone and glutenite and K-feldspar granite (Jg and Js-g) are distributed in the west and east of the study area. Cretaceous rhyolite porphyry and glutenite (Kr-g) are mainly exposed in the southwestern area. Sinian mica schist and quartz schist (Sn-s) and Cambrian quartz sand-

stone (ϵ) are observed in the middle part of the study area. The slope surface is mostly covered by residual soil and strongly weathered rock. Under the condition of rainfall, shallow landslides are mainly formed by loose deposits.

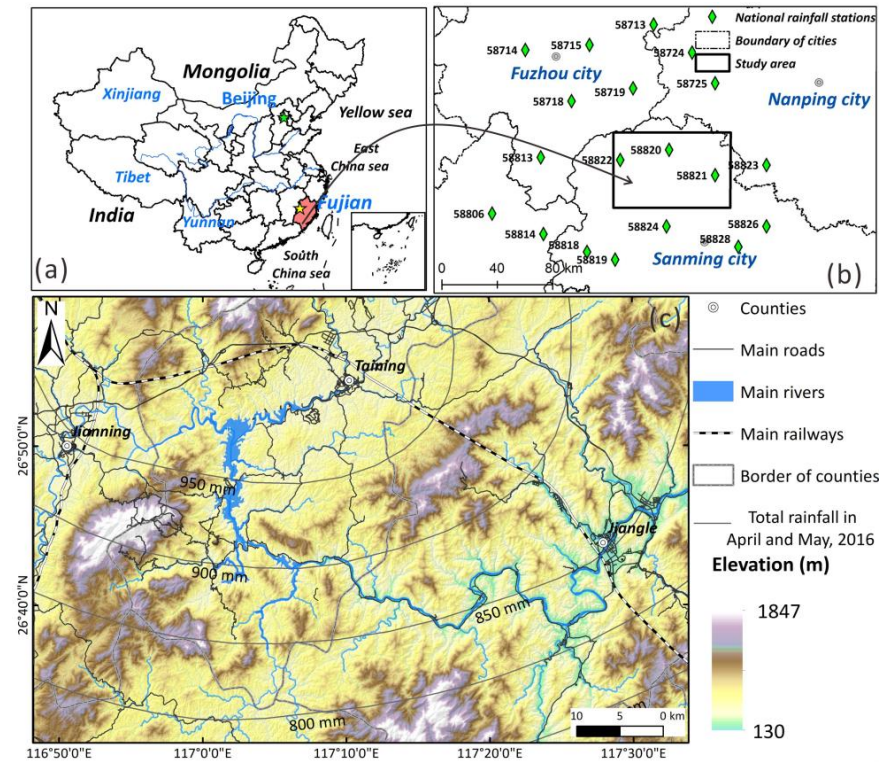


Figure 1. The geographical and topographical maps displaying the location and elevation distribution of the study area. (a) The location of Fujian Province; (b) the location of the study area and rainfall stations; and (c) the distribution of elevation, rainfall and water networks in the study area.

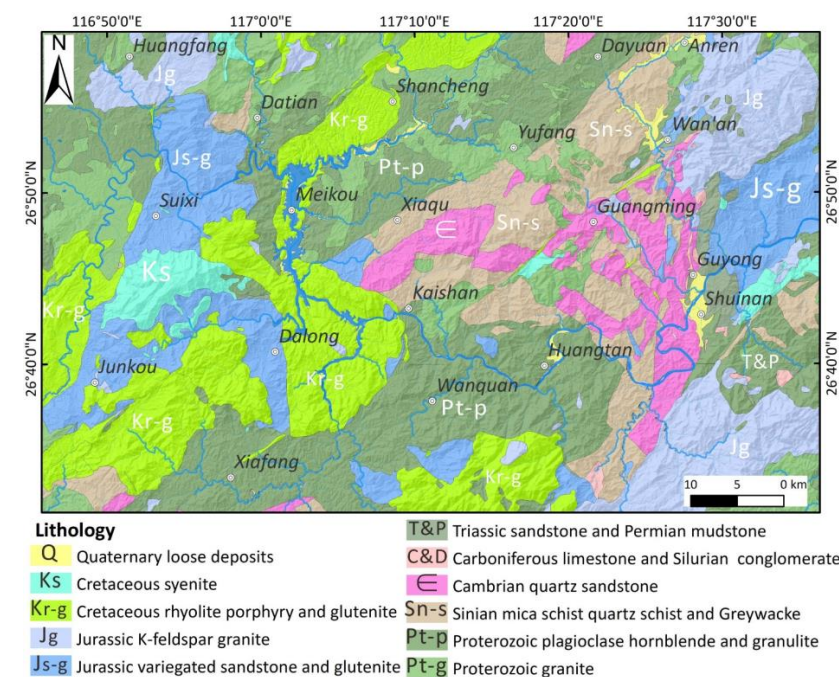


Figure 2. Lithology distribution of the study area. The geological map was created using China Geological Survey’s 1:200,000 geological maps (<http://dcc.cgs.gov.cn/>, accessed on 5 April 2023).

3. Data and Methods

3.1. Landslide Mapping

A comprehensive rainfall-induced landslide inventory is of significance for studying the distribution pattern of landslides, landslide susceptibility and their impact on geomorphological evolution. In this study, we were able to conduct a detailed visual interpretation of landslides due to the availability of high-resolution satellite photographs on the Google Earth (GE) platform [47,48]. The satellite images used for landslide interpretation were all based on the GE platform, which provided a 100% coverage of high-resolution satellite images. Due to the high vegetation coverage in the study area, optical images can be used to better identify the landslide locations before and after the events. By comparing the pre- and post-rainfall images combined with field investigations, the landslide inventory associated with this rainfall event was ultimately established. Figure 3 shows the field photos of landslides triggered by this event.

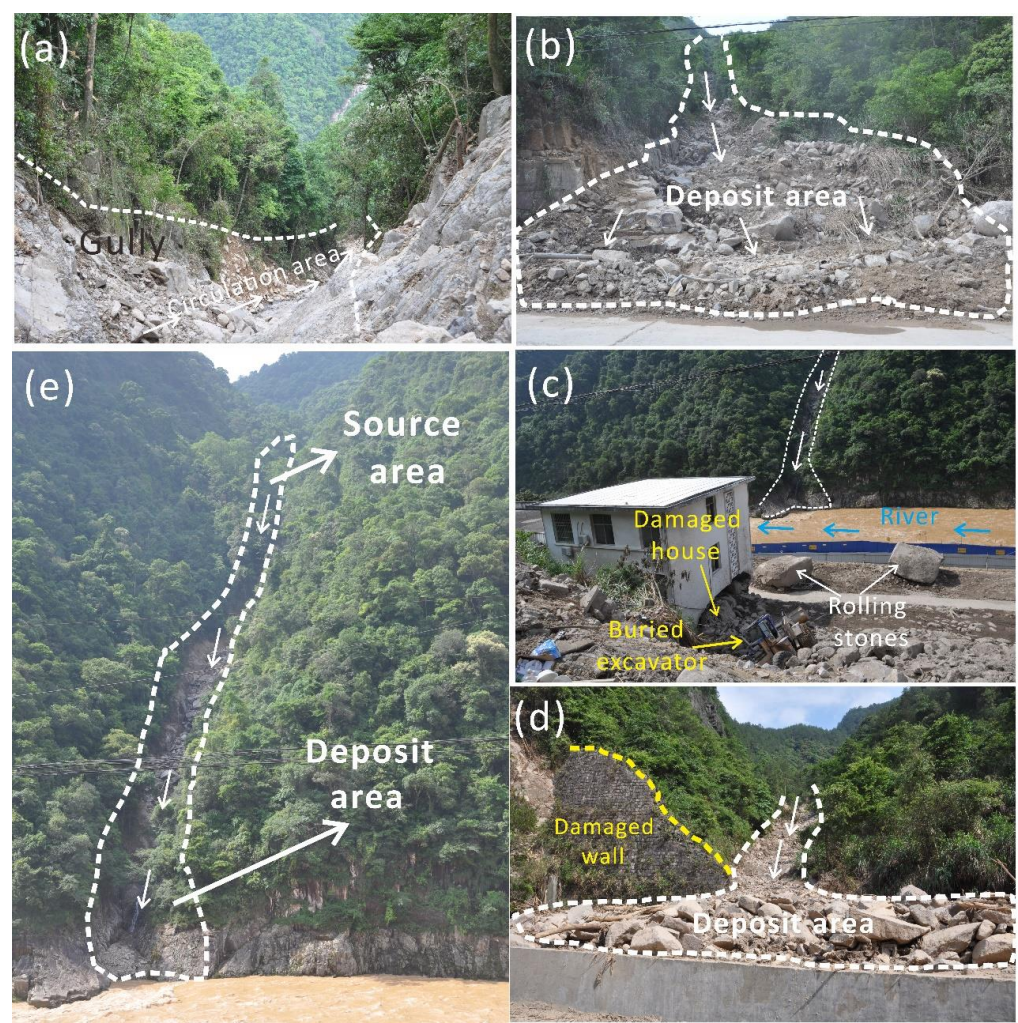


Figure 3. Field photos of landslides triggered by this rainfall event.

3.2. Rainfall Data

We collected precipitation data in the Sanming area for the last two decades (from 2000 to 2020). According to these data, the average annual rainfall in the Sanming area has remained between 1200–2400 mm, with prominent fluctuation. In 2016, the annual rainfall exceeded 2200 mm, while in 2003 the annual rainfall was relatively low, less than 1200 mm (Figure 4a). After comparison, we found that the rainfall in May 2016 was more than the monthly average rainfall over the past 20 years. The precipitation in May was 300 mm,

which is more than the average monthly rainfall in previous years (approximately 200 mm) (Figure 4b).

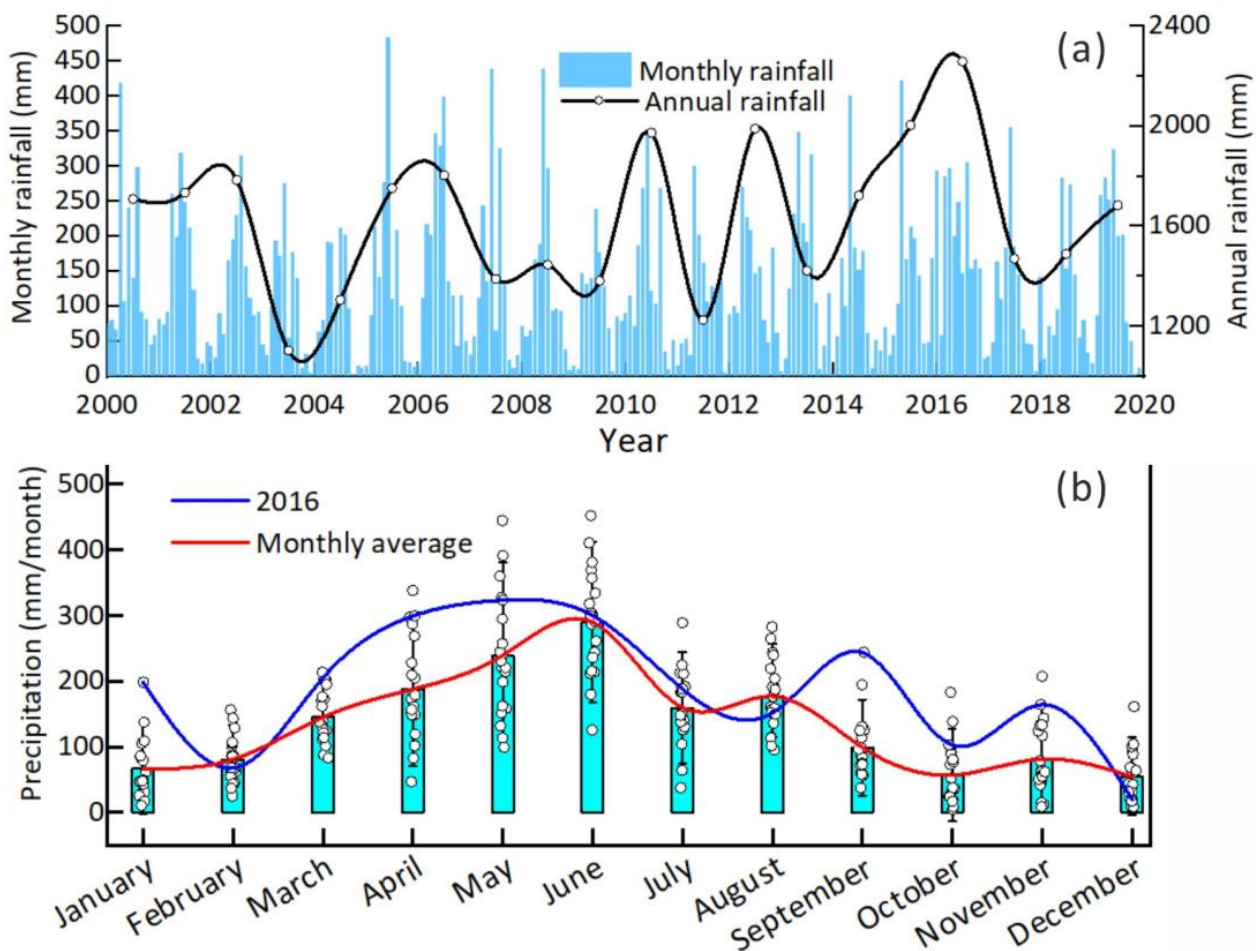


Figure 4. Monthly precipitation data of Sanming city over the past 20 years (2000–2020); (a) monthly and annual average precipitation data over the last 20 years; (b) comparison of the monthly rainfall in 2016 with the average precipitation over the last two decades.

We collected rainfall data from 19 rainfall stations of the China Meteorological Administration within a radius of 100 km in the study area. These stations recorded rainfall data every 12 h. Figure 5 shows the rainfall data from two stations located in the northern and western parts of the study area from 1 April to 30 May. Based on the rainfall data, we can observe that the rainfall event mainly occurred from 5 May to 10 May. The highest precipitation occurred on 8 and 9 May, reaching about 100–120 mm, which accounted for more than half of the total rainfall amount. The precipitation on the other four days was relatively low, averaging about 15–40 mm. Based on the above 19 rain gauges, the commonly used Kriging interpolation method was applied to obtain the distribution of the rainfall during different times of this event (Figure 6). The result indicates that the daily rainfall in the study area varies greatly, with a difference of around 160 mm on 8 May. In contrast, the spatial distribution of daily rainfall during other time periods shows relatively small variation, ranging from 10 mm to 40 mm.

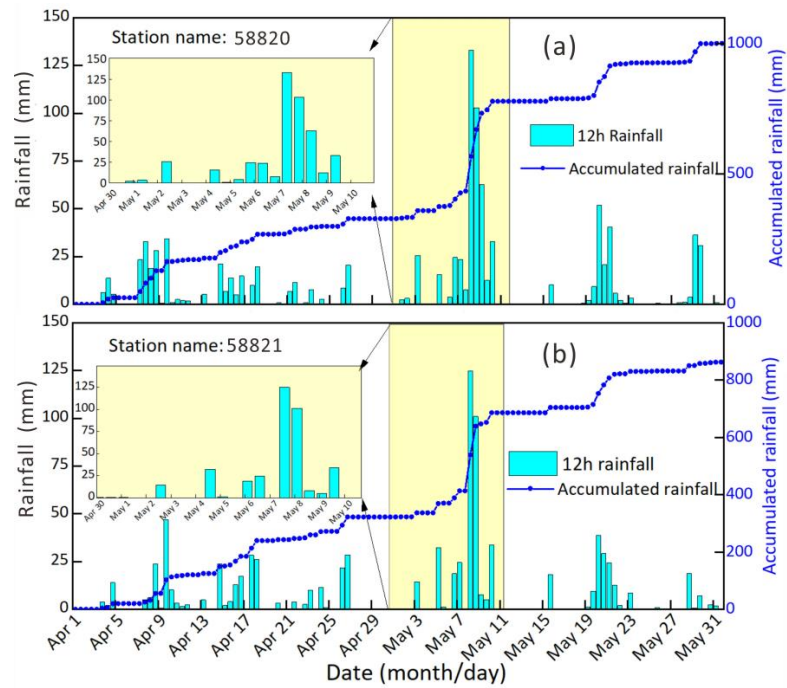


Figure 5. Precipitation data from every 12 h of two national stations in the study area from 1 April to 30 May; (a) the rainfall station (58,820) located in the north of the study area; (b) the rainfall station (58,821) located in the west of the study area.

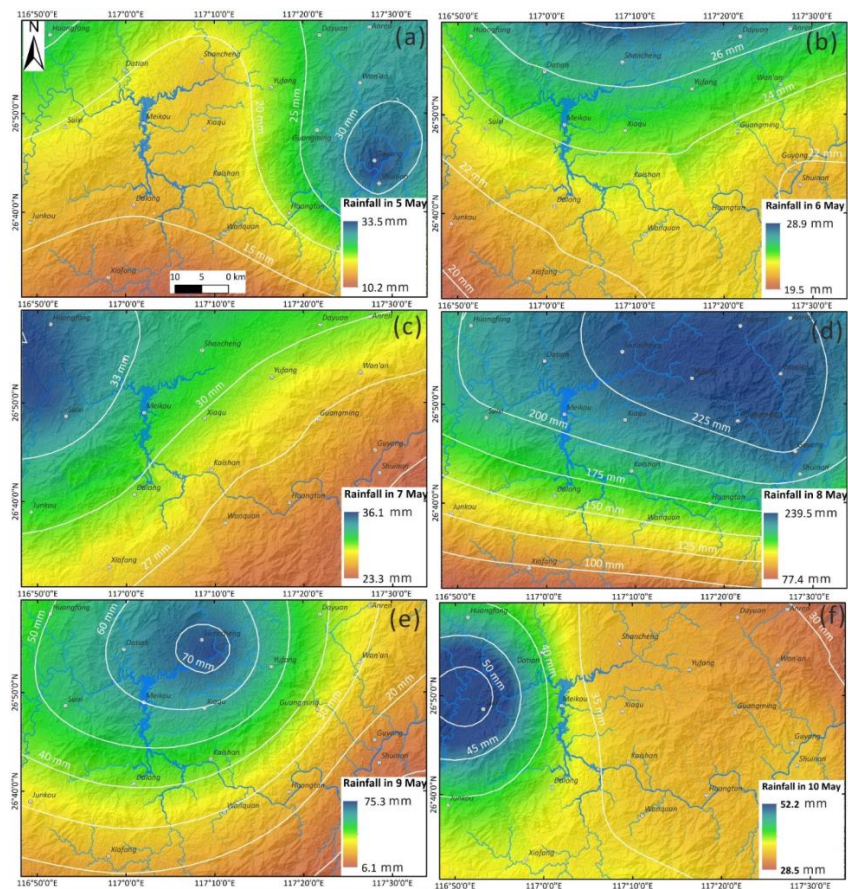


Figure 6. The spatial distribution of daily rainfall from 5 to 10 May during this rainfall event; (a) 5 May; (b) 6 May; (c) 7 May; (d) 8 May; (e) 9 May; (f) 10 May.

3.3. Data of Other Influencing Factors

Based on the distribution characteristics of landslides and influencing factors in the study area, as well as previous studies [9], we selected six factors, mainly including topography, geology, hydrology, land cover and rainfall. The ALOS PALSAR DEM data with a resolution of 12.5 m was used to calculate the hillslope gradient and slope aspect. We calculated the topographic relief based on the elevation range within a 1.0 km radius. TWI was calculated using GRASS GIS software and elevation data and drainages were derived from the DEM using ArcGIS software. The land use type data was derived from the 10 m resolution global land cover results [49]. Finally, all influencing factor layers were divided into 12.5×12.5 m grids and subjected to statistical analysis (Figure 7).

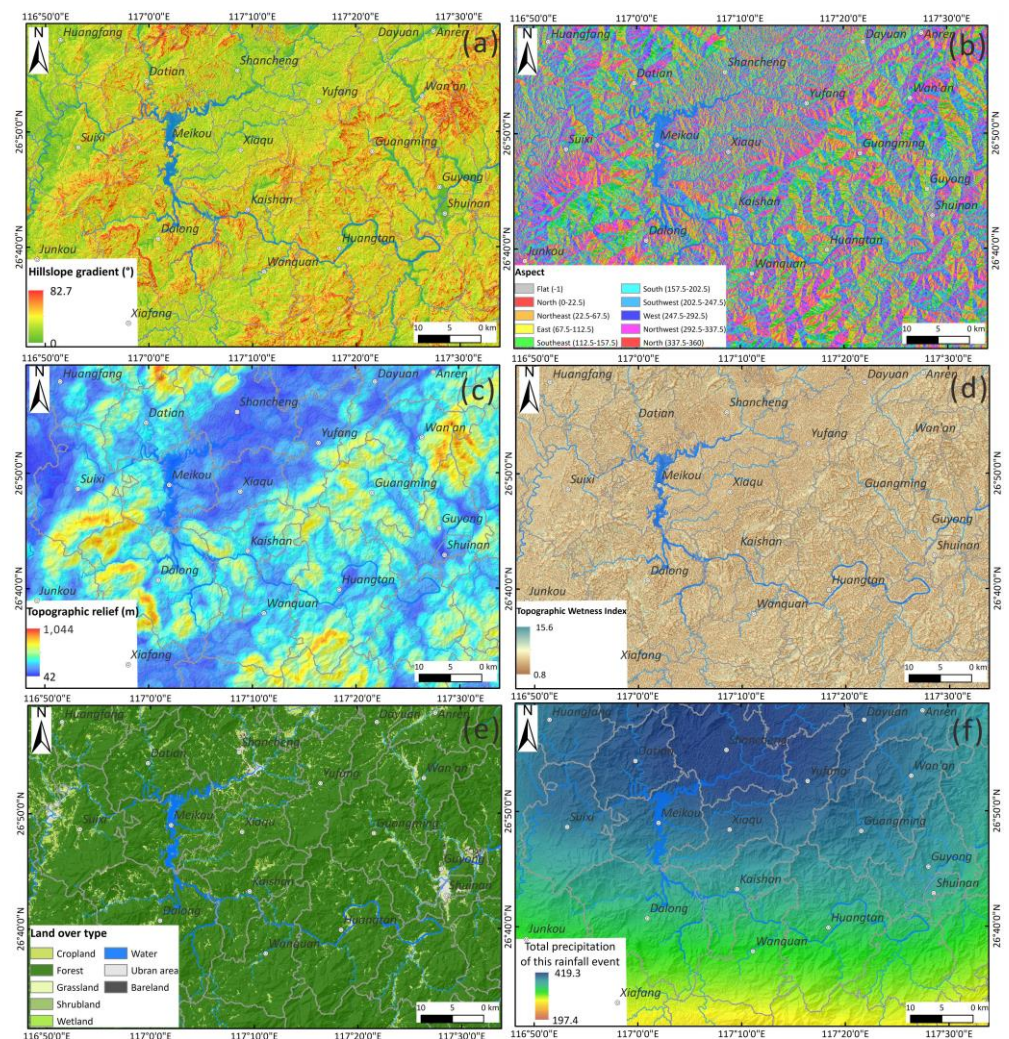


Figure 7. Map showing the spatial distribution of the influencing factors; (a) hillslope gradient; (b) aspect; (c) topographic relief; (d) topographic wetness index; (e) land over type; (f) total precipitation of this event.

3.4. TRIGRS Modelling

The TRIGRS model (transient rainfall infiltration and grid-based regional slope-stability model) is programmed by the USGS (United States Geological Survey) [50,51] and is widely used for evaluating shallow-rainfall-induced landslide susceptibility [52,53]. Specific input data are required such as rainfall, soil mechanics and hydrological characteristics of the study area [50]. After determining these parameters, using a GIS platform, the model calculates grid stability as a result of the change in transient pore water pressure of each grid during the rainfall period. Iverson [54] linearized the Richards equation solution,

which serves as the foundation for infiltration models for moist beginning circumstances with steady and transient seepage components. The former is governed by the water table’s initial depth and constant infiltration rate, which maintains slope stability. The latter refers to the increase in pore water pressure caused by rainfall, which can cause instability. The generalized solution in TRIGRS is

$$\begin{aligned} \psi(Z, t) = & (Z - d)\beta + 2\sum_{n=1}^N \frac{I_{nz}}{K_s} H(t - t_n) [D_1(t - \\ & t_n)]^{\frac{1}{2}} \sum_{m=1}^{\infty} \left\{ ierfc \left[\frac{(2m-1)d_{LZ} - (d_{LZ} - Z)}{2[D_1(t - t_n)]^{\frac{1}{2}}} \right] + ierfc \left[\frac{(2m-1)d_{LZ} + (d_{LZ} - Z)}{2[D_1(t - t_n)]^{\frac{1}{2}}} \right] \right\} - \\ & 2\sum_{n=1}^N \frac{I_{nz}}{K_s} H(t - t_{n+1}) [D_1(t - t_{n+1})]^{\frac{1}{2}} \sum_{m=1}^{\infty} \left\{ ierfc \left[\frac{(2m-1)d_{LZ} - (d_{LZ} - Z)}{2[D_1(t - t_{n+1})]^{\frac{1}{2}}} \right] + \right. \\ & \left. ierfc \left[\frac{(2m-1)d_{LZ} + (d_{LZ} - Z)}{2[D_1(t - t_{n+1})]^{\frac{1}{2}}} \right] \right\} \end{aligned} \tag{1}$$

where ψ denotes pressure head; t is rainfall time; N is the number of rainfall time intervals; Z is the depth below the surface; d is the depth of water table; d_{LZ} indicates the impervious basement border depth; $\beta = \cos^2\delta - (I_{ZLT}/K_s)$, δ is the hillslope gradient; I_{ZLT} is the constant surface flux; K_s is the saturated hydraulic conductivity; I_{nz} is the n th time period, surface flux; $D_1 = D_0/\cos^2\delta$, D_0 is the saturated hydraulic diffusivity and $H(t - t_n)$ is the Heaviside step function in which t_n is the time at the n th time interval in the rainfall sequence.

$$ierfc(\eta) = \frac{1}{\sqrt{\pi}} \exp(-\eta^2) - \eta erf(\eta) \tag{2}$$

where $erfc(\eta)$ denotes the complementary error function.

The TRIGRS model computes infiltration (I) for each cell by adding precipitation (P) and any runoff from upslope cells (R_u). However, it is important to note that the saturated hydraulic conductivity (K_s) cannot be exceeded by infiltration. This ensures that the model accounts for the limitations of soil permeability.

$$I = P + R_u, \text{ if } P + R_u \leq K_s \tag{3}$$

$$I = K_s, \text{ if } P + R_u > K_s \tag{4}$$

when $P + R_u$ surpasses K_s in a cell, the surplus is referred to as runoff (R_d) and it is directed to neighboring downslope cells.

$$R_d = P + R_u - K_s, \text{ if } P + R_u - K_s \geq 0 \tag{5}$$

$$R_d = 0, \text{ if } P + R_u - K_s < 0 \tag{6}$$

The TRIGRS model computes slope stability using an infinite-slope stability analysis (Equation (7)), as explained in Iverson [54]. In this analysis, it is the percentage of resistive basal Coulomb friction in the presence of gravitationally produced downslope. The instability of an infinite slope is characterized by basal driving stress [55]. The TRIGRS model calculates this ratio, known as the FoS , at depth Z by

$$FoS(Z, t) = \frac{\tan\phi'}{\tan\delta} + \frac{c' - \psi(Z, t)\gamma_w \tan\phi'}{\gamma_s Z \sin\delta \cos\delta} \tag{7}$$

where c' is the soil cohesion; ϕ' is the friction angle of the soil; γ_s is the unit weight of soil and γ_w is the unit weight of groundwater.

To overcome the difficulties associated with manually updating several model parameters and sophisticated data processing in the standard TRIGRS model, Ma et al. [56]

posed a new TRIGRS model using Matlab[®] programming. This model can directly read grid data in TIF format as input and output prediction results, greatly simplifying data preparation and parameter configuration. It includes two script files, INPUT DATA.m and TRIGRS.m. The TIF input files are read by the INPUT DATA.m file, whereas TRIGRS.m is the executable program that calculates the pressure head and FoS. By computing the pressure head and FoS at various soil depths, the model provides the minimum FoS and accompanying pressure head in TIF format. More information may be found in [56]. The flow chart of this study is shown in Figure 8.

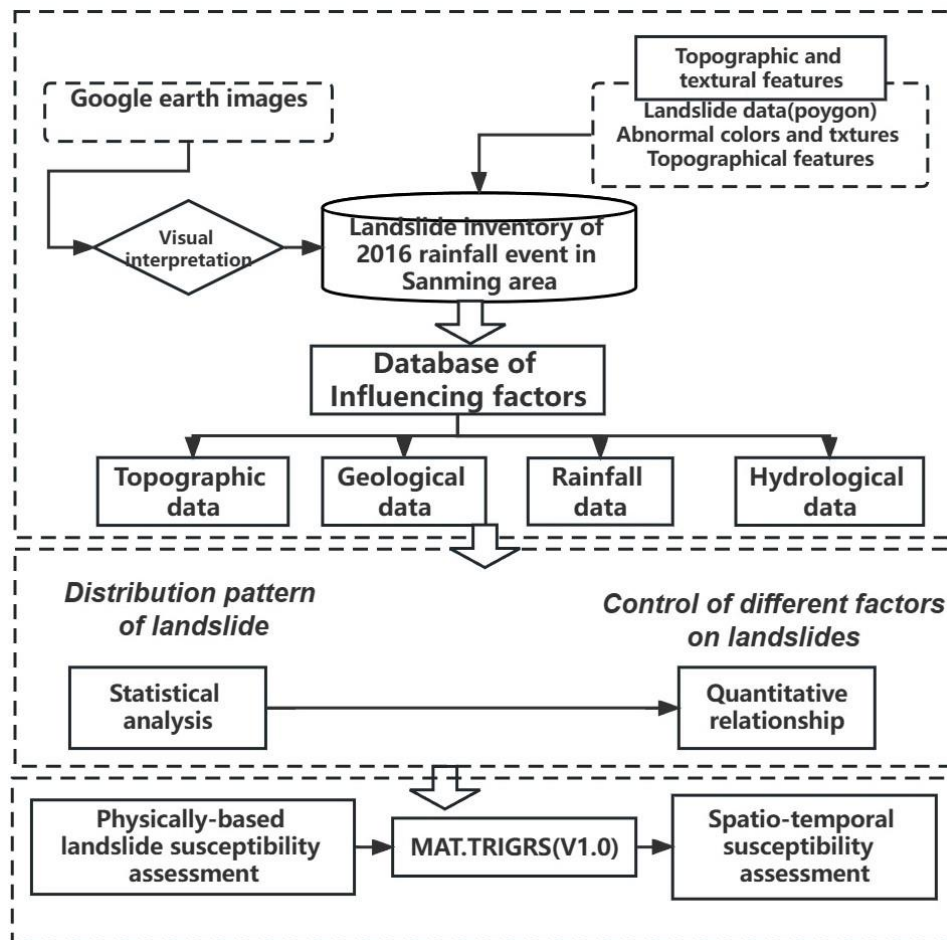


Figure 8. Flow chart of this study.

4. Results

4.1. Basic Characteristics of Rainfall-Induced Landslides

Based on the detailed landslide database of this rainfall event, it is clear that approximately 2665 landslides were triggered by this event (Figure 9a). The landslides were mostly small-scale shallow landslides with an elongated type. Among them, the largest landslide has an area about 50,000 m², while the smallest one is only 36 m², with an average area of 1070 m². The number of landslides with an area greater than 10,000 m² is 6. Approximately 21 landslides have an area between 5000–10,000 m² and 927 landslides have an area between 1000–5000 m². However, the majority of landslides (1711) possess an area of less than 1000 m². We used a moving window with a radius of 2.5 km and a Gaussian density kernel function to calculate the landslide number density (LND) in the study area (Figure 9b). The results show that the maximum LND reaches over 80/km². Spatially, the landslides are mainly concentrated in the northern part of Xiaqu town and the southern part of Yufang town.

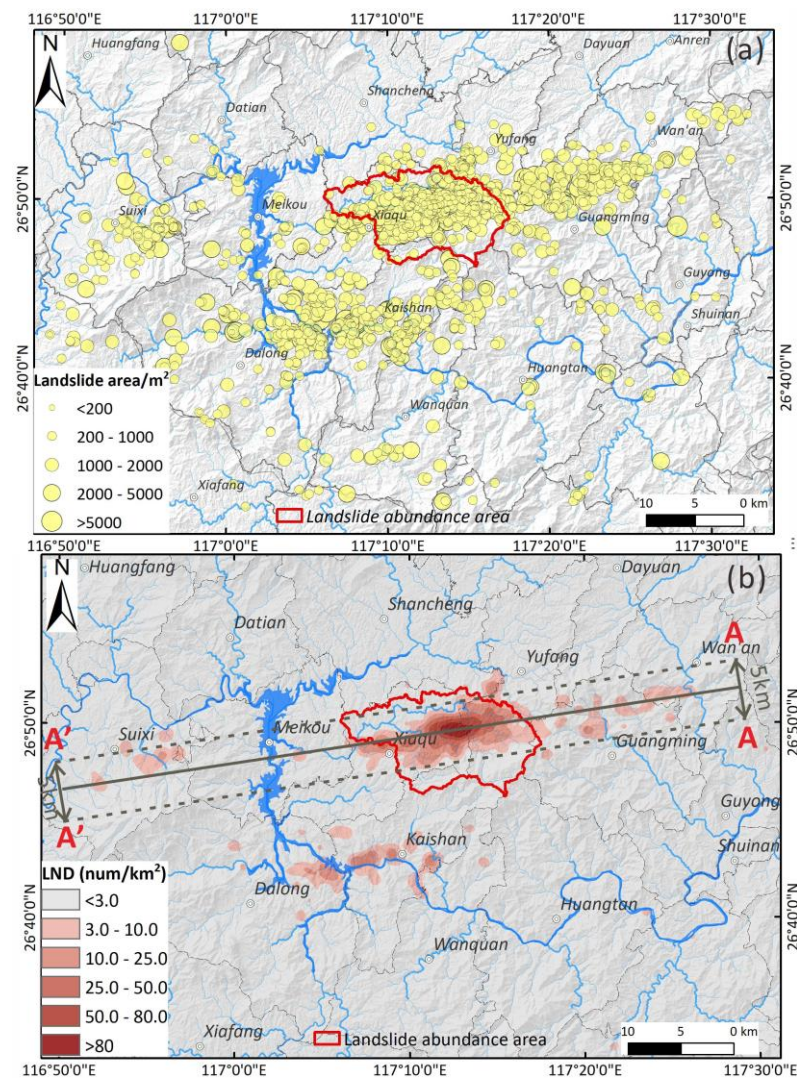


Figure 9. Spatial distribution of landslides and landslide number density (LND). (a) Inventory of the rainfall-induced landslides (b) landslide number density (LND); the red line delineates the landslide abundance area.

4.2. Correlation between Landslides and Influencing Factors

To analyze the relationship between the influencing factors and landslide occurrence, we conducted a statistical analysis of the frequency distribution of landslides and landscape (non-landslide) areas under different intervals, as well as landslide area density (LAD) under different intervals. Figure 10 shows the frequency density distribution of landslides and landscape areas under different influencing factors. Figure 11 shows the LAD distribution of six influencing factors under different intervals. Higher LAD values indicate the areas that are more prone to landslides. The results show that for elevation, most landslides are concentrated between 300–500 m. The landslide frequency density reaches a maximum of 0.22 in the elevation interval of 370–430 m. As for the hillslope gradient, most landslides are concentrated in the interval of 15–25°, with an average slope of 21.7°. Both landslide and non-landslide areas have the highest frequency density in the slope interval of 14–18° and the values are 0.15 and 0.16, respectively. The same distribution pattern can also be observed in TWI. Specifically, the landslide frequency density reaches its maximum near 4.5, with a value of 0.36. As for topographic relief, non-landslide areas are mainly concentrated between 300–500 m, while landslide areas are mainly concentrated between 150–200 m. For distance to a river, most landslides are concentrated within 800 m, which is the area most affected by river erosion. In the aspect of total rainfall, landslides

are predominantly concentrated in the region with annual rainfall intervals of 320–330 mm and 380–400 mm, with landslide frequency densities of 0.1 and 0.36, respectively.

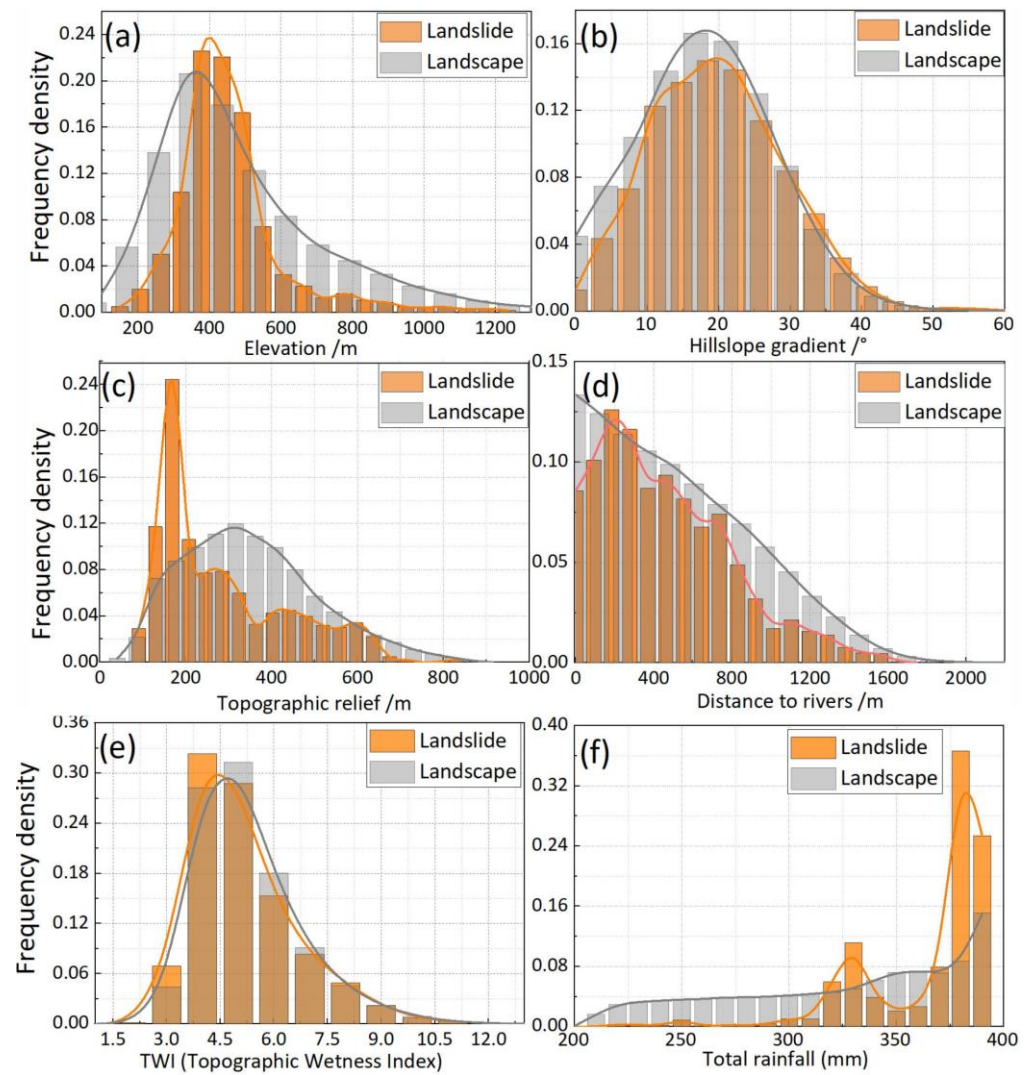


Figure 10. Frequency density estimates of landslide and landscape areas of six influencing factors; (a) elevation; (b) hillslope gradient; (c) topographic relief; (d) distance to river; (e) topographic wetness index (TWI); (f) total rainfall.

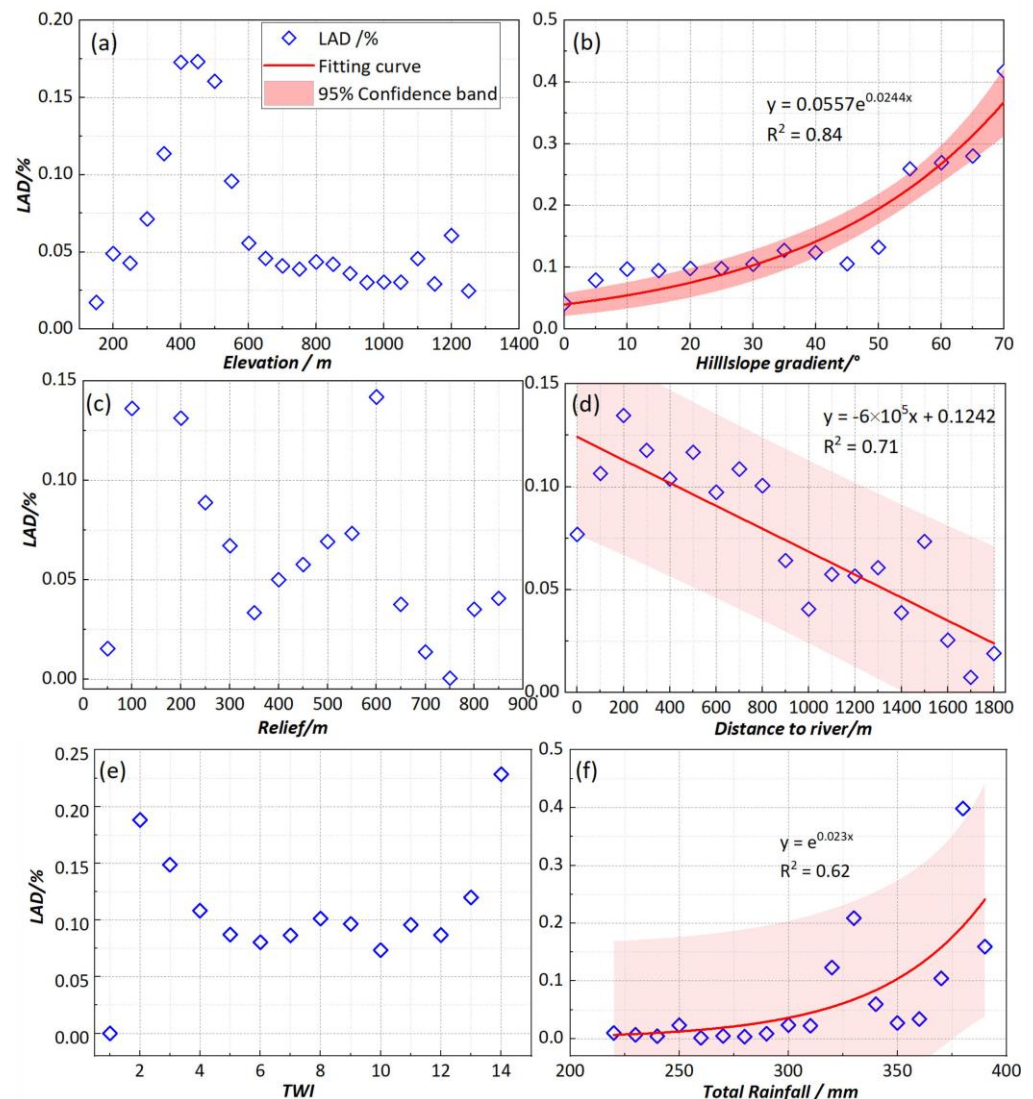


Figure 11. The relationship between the landslide areal density (LAD) and six influencing factors; (a) elevation; (b) hillslope gradient; (c) topographic relief; (d) distance to river; (e) topographic wetness index (TWI); (f) total rainfall.

Based on the statistical relationship between LAD and different influencing factors (Figure 11), it is observed that there is no significant correlation between elevation, relief, TWI and landslide abundance index. For elevation, the highest LAD (0.17%) is observed in the elevation range of 400–450 m, while the maximum LAD (0.13%) is observed in the relief range of 100–200 m and 550–650 m. By comparison, a tight correlation is seen between LAD and the other three influencing factors (i.e., hillslope gradients, distance to river and total rainfall). For hillslope gradient, the LAD increases with an increase in hillslope gradient and is described by an exponential relationship: $y = 0.0557e^{(0.0244x)}$, where x is the hillslope gradient and y is the LAD (Figure 11b). The equation indicates that with the increase in hillslope gradient, the possibility of landslide occurrence also raises. In terms of distance to a river, there is a negative linear relationship between the LAD and distance to a river: $y = -6 \times 10^5 x + 0.124$, where x represents the distance to a river and y is the LAD (Figure 11d), indicating that the LAD decreases with the increase in distance to rivers. For total rainfall, the LAD and total rainfall show an exponential relationship: $y = e^{0.023x}$, where x is the total rainfall and y is the LAD. Such a relationship demonstrates that landslides are more likely to occur in areas with high precipitation (Figure 11f).

Figure 12 shows the areal coverage (%) of various lithological types for landslide and landscape area, overlaid by the average landslide area and LAD estimated per unit. The result shows that the predominant lithology is protozoic plagioclase hornblende and granulite (Pt-p), which account for 25% of the study area, followed by Cretaceous rhyolite porphyry and glutenite (Kr-g), which account for more than 15% of the study area. Among all lithological types, Sinian mica schist and quartz schist (Sn-s) are the most prone to landslides, with over 35% of landslides occurring in 10% area. Furthermore, statistics on the average landslide area of different lithological units show that Kr-g and Pt-p have the largest average landslide area (>1400 m²), followed by Cambrian quartz sandstone (€), which has an average landslide area of 1200 m². Quaternary loose deposits (Q) have a small average landslide area, only 600 m².

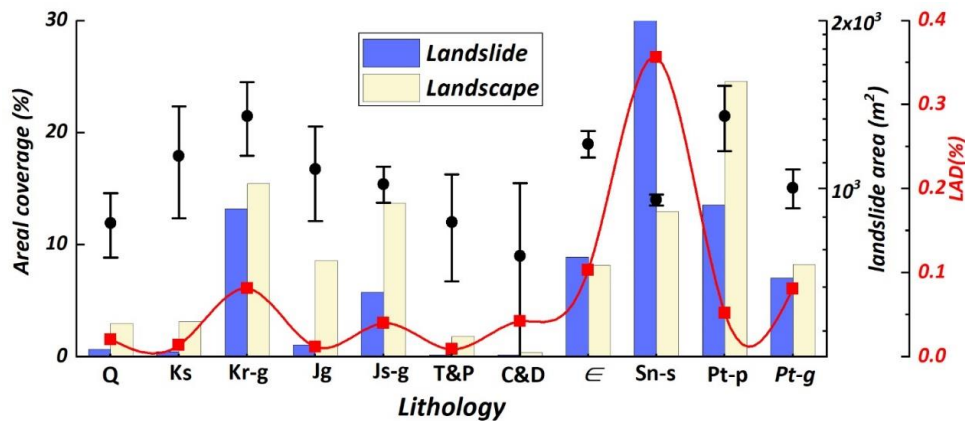


Figure 12. Areal coverage (%) of various lithological types for landslide and landscape, overlaid by average landslide area and LAD estimated per unit.

Based on the frequency density distribution and statistical analysis of landslide area density (LAD) across various aspects in both landslide and non-landslide areas, we found that the landslides on E-SE oriented slopes are highly developed, particularly within a slope aspect of 60–100°. The statistical results further revealed that landslide area density (LAD) was highest within the 50–110° range, reaching 0.17%. Overall, the eastern aspect of the area displayed a greater concentration of landslides, while the western slope exhibited lower levels of landslide development (Figure 13).

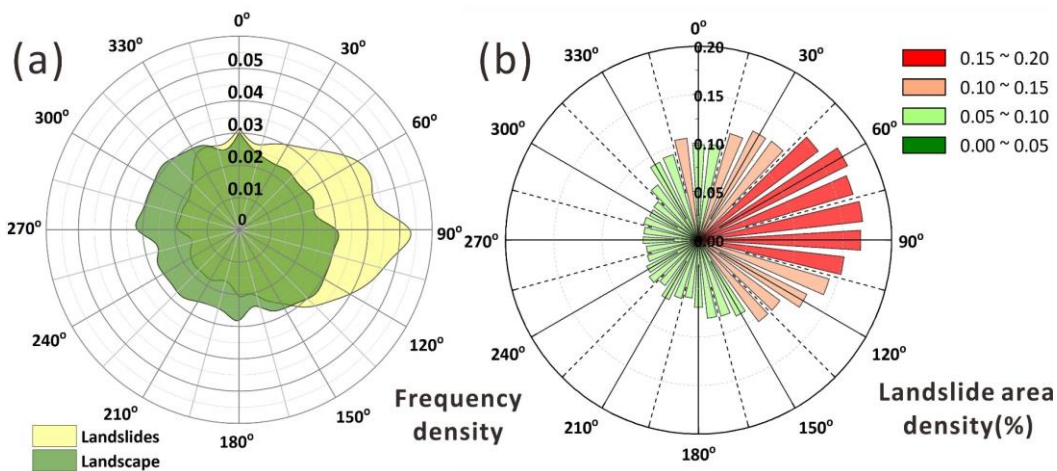


Figure 13. (a) The distribution of aspect within landslide and landscape areas; (b) correlations between aspect and LAD.

4.3. Spatio-Temporal Susceptibility Assessment

To achieve accurate landslide spatiotemporal susceptibility results using physically based models, obtaining sufficient and correct input parameter data is the foremost requirement [30,52,57,58]. The Z-model of Saulnier et al. [59] was used to evaluate the thickness of weathered soil mass. We assumed that the weathered soil mass covered by the upper layer of bedrock has a maximum thickness of 5 m and a minimum thickness of 0.5 m, as determined by previous studies [60,61]. Therefore, the estimation of soil thickness based on altitude can be calculated using Equation (8).

For landslide abundance areas, the lithology in the study area mainly includes Proterozoic granite (Pt-g), Sinian mica schist and quartz schist (Sn-s), Cambrian quartz sandstone (ϵ) and Quaternary loose deposits (Q). Based on previous studies [9,23,62] and rock engineering standards used in China [63], we assigned the corresponding values to hydrological and mechanical parameters, including soil cohesion (c'), internal friction angle (ϕ'), unit weight (γ_s) and saturated hydraulic conductivity (K_s) for different lithological types. Specific mechanical and hydrological parameter assignments for different lithologies can be found in Supplementary Materials Table S1. Otherwise, based on previous experience [44,64], saturated hydraulic diffusivity D_0 was set to $200K_s$ and the initial surface flux (I_{ZLT}) is generally less than K_s to one power or more and was often set to $I_{ZLT} = 0.01K_s$.

$$h_i = h_{max} - \left(\frac{Z_i - Z_{min}}{Z_{max} - Z_{min}} \right) (h_{max} - h_{min}) \quad (8)$$

where Z_{max} and Z_{min} refer to the maximum and minimum thicknesses of weathered soil mass, respectively. h_{max} and h_{min} are the maximum and minimum altitudes, respectively.

Figure 14 shows the predicted pictures of the FoS based on rainfall data over different time periods. From the results, it can be observed that prior to the rainfall, most of the study area had an FoS greater than 1.2. As the rainfall event began, unstable areas with an FoS less than 1.2 (shown in the red area) mainly appeared on both sides of the gullies and, by 8 am on 7 May, the unstable area within the study area rapidly increased. After 12 h of rainfall (reaching a rainfall amount of 102 mm) on 8 May at 8 am, the unstable area (shown in the red area) reached its critical value. Although several subsequent intermittent rainfall events occurred, the impact of rainfall on the change in the FoS was tiny and ignorable and the unstable area remained unchanged. We compared the prediction accuracy of the simulation results over different time periods based on the ROC curve. As shown in Supplementary Materials Figure S1, the prediction ability of the assessment results in different time periods varied between 0.68 and 0.72. Among them, the evaluation results on the 7 and 8 June had the highest prediction accuracy, around 0.72.

We conducted a statistical analysis on the temporal variations of the FoS results for different hillslope gradients during different time periods. Figure 15a shows the variations in the FoS of the grids with gradients less than 30° , where the majority of the FoS ranged from 1.8 to 2.4 with an average of approximately 2.1 before the onset of rainfall. As heavy rainfall occurred, the FoS gradually decreased and the average FoS reached around 1.95 at 8:00 on 7 May. Subsequently, the occurrence of intense rainfall on 8 May resulted in a significant decrease in the FoS for the grids with gradients less than 30° , with the average FoS maintained at around 1.85. Despite the persistent rainfall in the later period, the overall variation in the FoS for most grids was small, with an average of approximately 1.8. Similar phenomena were observed for the grids with gradients greater than 30° (Figure 15b). Prior to the rainfall, the FoS for these grids were basically distributed between 1.4 and 1.7, with an average of approximately 1.6. As rainfall increased, the FoS continued to decrease and after the intense rainfall event on 8 May, most of the shallow weathered soil layers became saturated. As a result, the FoS reached critical values and maintained between 1.1 and 1.4, with an average of approximately 1.3. Although the rainfall continued to occur, the impact of rainfall on the FoS was small due to the saturated state of the soil layers and the FoS for the grids remained stable.

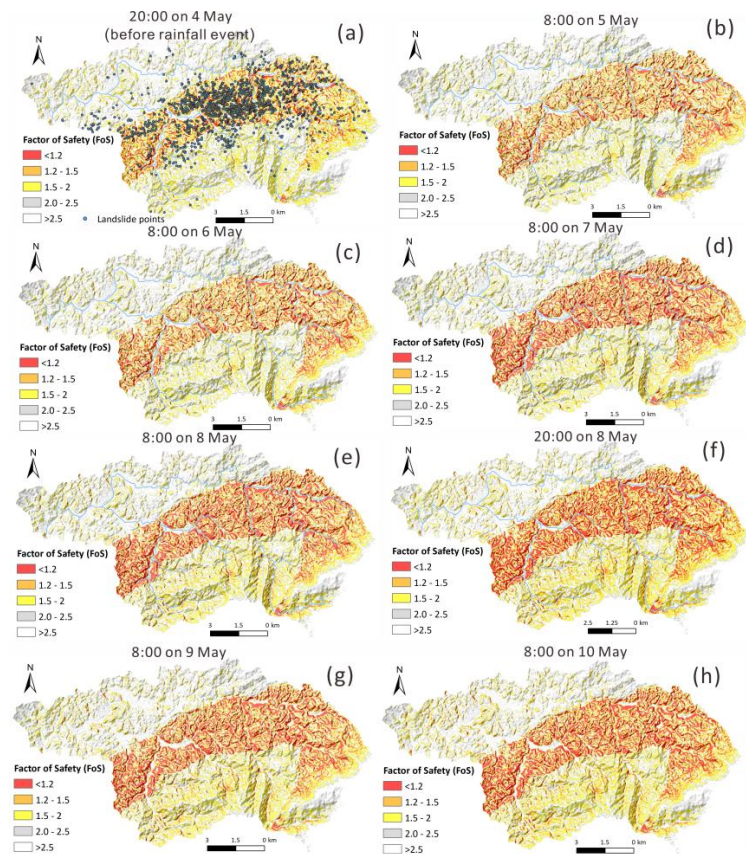


Figure 14. Conditions for slope stability, as measured by the factor of safety (FoS) at different times during the 2016 rainfall event; (a) 20:00 on 4 May (UTC + 8, before rainfall event); (b) 8:00 on 5 May (UTC + 8); (c) 8:00 on 6 May (UTC + 8); (d) 8:00 on 7 May (UTC + 8); (e) 8:00 on 8 May (UTC + 8); (f) 20:00 on 8 May (UTC + 8); (g) 8:00 on 9 May (UTC + 8); (h) 8:00 on 10 May (UTC + 8).

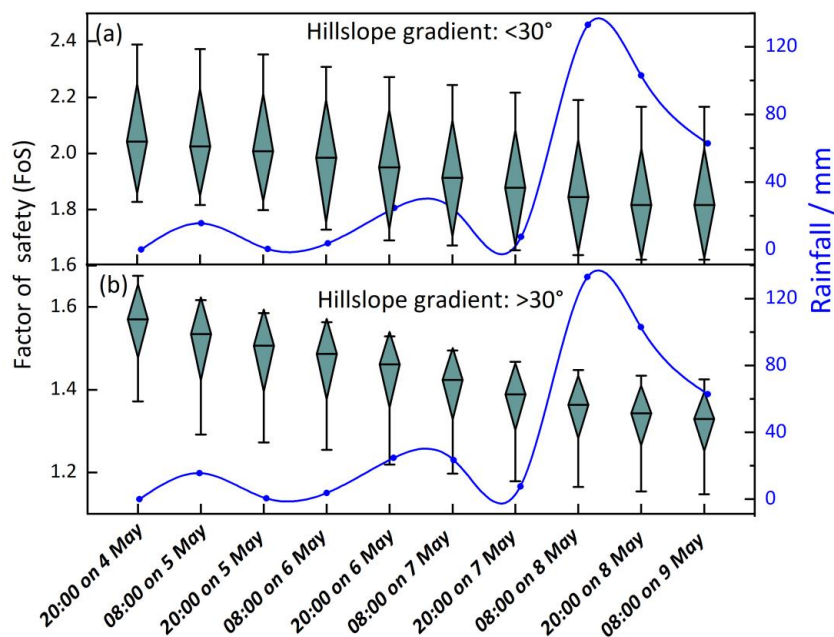


Figure 15. FoS results for various hillslope gradient intervals at different rainfall times; (a) hillslope gradient: $<30^\circ$; (b) hillslope gradient: $>30^\circ$.

5. Discussion

Topography, geological features and rainfall characteristics are considered to be essential factors influencing the occurrence of rainfall-induced landslides [65–67]. It is generally accepted that steeper terrain, weaker rock strength and higher rainfall amounts increase the occurrence likelihood of landslides [17,68,69]. To better understand the spatial distribution of the rainfall-induced landslides with different elevations, hillslope gradients, topographic relief, lithological types and rainfall characteristics, the swath profiles (EEN-WWS) with a width of 10 km are presented (Figure 16). The spatial distribution of landslides shows that the majority of the landslides are concentrated in Xiaqu town, which has the maximum landslide number density ($100/\text{km}^2$). In terms of topography, the Xiaqu area belongs to the transitional zone from high to low altitude, with an elevation generally ranging from 400 to 600 m. The hillslope gradients in this area are small, with a range from 10° to 30° and an average gradient of 20° . Regarding the rainfall distribution, the Xiaqu area is located in the region with the highest precipitation of nearly 400 mm. Thus, the spatial distribution of landslides is strongly controlled by the rainfall characteristics (Figures 16 and 10f). Otherwise, the primary rock type in the Xiaqu area is Sinian mica schist and quartz schist (Sn-s) and the statistical results show that over 35% of landslides are distributed in the area with this lithological type (Figure 12). We suggest that the schist belongs to metamorphic rock, which is influenced by geological structure, tectonics and mineral composition. When schist is in contact with water, characteristics such as creep, mechanical anisotropy, softening and deterioration may be observed. Due to these unique properties, schist in mountainous areas often experiences frequent landslides [70,71]. For the study area, mica schist and quartz schist have well-developed cleavage and high mica content. Meanwhile, due to the long-term physical weathering, the rock mass on the surface of the bedrock is fragmented, with highly developed fissures and locally filled mud. Therefore, this lithological type is prone to the development of weak structural layers after long-term immersion of rainfall, thereby providing a natural sliding surface for landslides [72]. Additionally, due to the development of cracks in the weathered rock and soil, long-term rainfall can penetrate through the cracks and increase pore water pressure in the rock mass and the decreased shear resistance caused by increased self-weight of the rock mass is also one of the main reasons for the occurrence of landslides.

In the southeast coastal area, orographic amplification of rainfall and the projection of rainfall-vector on hillslopes might result in greater rainfall in the windward hillslopes, resulting in a higher incidence of landslides on the hillslope scale [73]. During the summer months (June and July), the Sanming area is dominated by the southeast monsoon, which is influenced by the monsoon depression and tropical cyclone. The distribution of landslides during this rainfall event indicates that hillslopes facing southeast and east are more susceptible to collapse than those facing northwest-north (Figure 13). This phenomenon can be mainly attributed to the fact that the south-oriented slopes are predominantly windward, leading to greater rainfall and splash erosion.

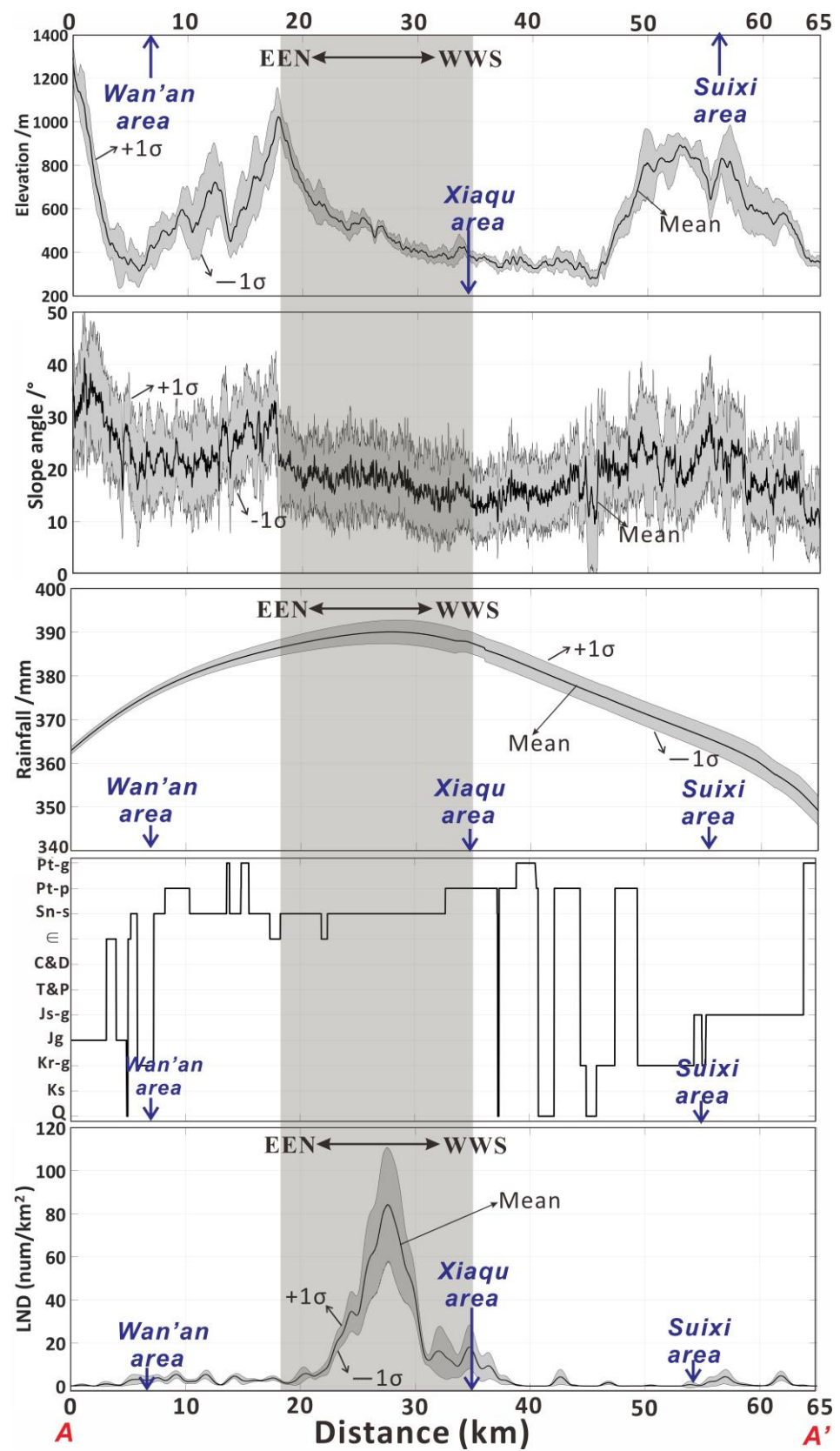


Figure 16. Comparison of longitudinal (EEN-WWS) swath profiles of elevation, slope angle, rainfall, lithology and LND; the location of the swath profile is shown in Figure 8.

In addition, we collected the landslide data and the corresponding population statistics from different towns (Figure 17). According to the statistical results, we found that the landslide size in each town was similar, with most landslides ranging from 600 to 1000 m². Hangtan, Guangming and Yunkou towns had relatively larger average landslide areas, reaching 1000 m² (Figure 17). In terms of the relationship between landslide numbers and population distribution in each town, we can observe that the towns with the most concentrated landslides were areas with the lowest populations (Figure 17). For example, more than 1000 landslides occurred in Xiaqu town but the local population is only 7000. Yufang town had nearly 600 landslides, but the population is only around 2700. On the other hand, areas with fewer landslides corresponded to regions with more concentrated populations, such as Guyong and Shancheng towns, which had populations of 50,000 and 45,000, respectively, but only around 50 landslides occurred in each town. By comparing the topography, geomorphology and rainfall characteristics of these towns, we found that Yufang and Xiaqu towns were located in an area with the highest rainfall intensity and the most susceptible strata for landsliding. In contrast, Guyong and Shancheng towns had gentler terrain, with most hillslope gradients being less than 15°, making them low-susceptibility areas for landsliding. Although these areas are considered low-susceptibility areas, the loss of people's lives and property is still possible due to the landslides triggered by typhoons and heavy rainfall events. Conversely, although Yufang and Xiaqu towns are considered high-susceptibility areas for landsliding, their low population density may result in a lower impact on residents and public facilities.

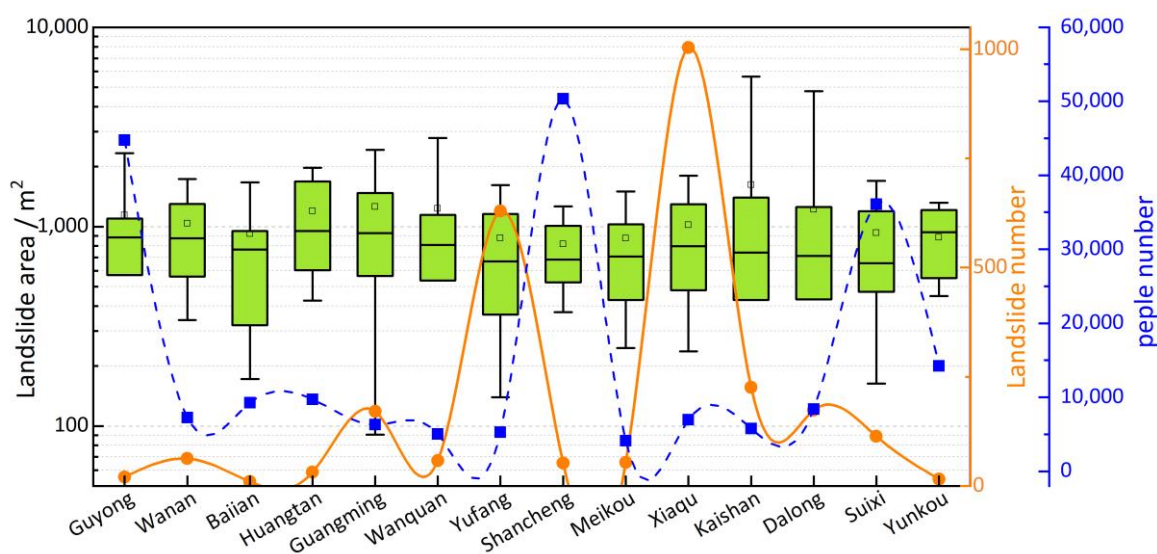


Figure 17. Landslide scale, number of landslides and the corresponding population distribution in different towns of the study area.

We calculated the antecedent precipitation index (API) of the study area with different statistical steps (5, 10, 15 days) based on the daily precipitation data (Figure 18). The relevant information about the API is detailed in the Supplementary Materials. From 1 April to 16 May, three API curves were all in the high-value range, with peaks occurring around 10 April, 20 April and 10 May, respectively. The first two peaks had relatively smaller API values (90 mm and 80 mm), while the largest peak appeared around 10 May. The Sanming area witnessed a strong rainstorm from 5 May to 10 May, with a total precipitation of 250 mm within 24 h and a maximum rainfall intensity of 56.6 mm/h. During this time, the API curves increased significantly and reached their pinnacle (250–280 mm). Subsequently, as the rainfall events ceased, the API rapidly decreased. In summary, the preceding rainfall events with low intensity (before 5 May) increased the soil water content and the short

duration of heavy rainfall on 8 May caused the rapid saturation of soil water content, thus leading to the occurrence of massive landslides in the Sanming area.

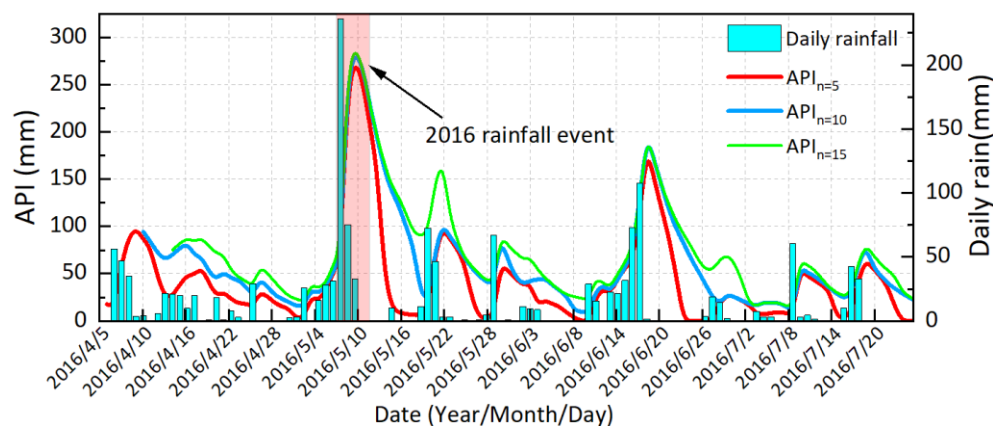


Figure 18. The rainfall data and calculated antecedent precipitation index (API) of this rainfall event.

In physically based models, accurate input information is essential to obtain accurate simulation results [58,74]. However, obtaining accurate input parameters for rock and soil is a challenging task in actual situations, so input data differ from the actual situation to some extent. For example, there is spatial heterogeneity in the mechanical parameters of different positions on slope body and the mechanical and hydrological parameters may be different at various depths [75]. In addition, the evaluation scale based on physically based models is a large area, which is limited by sampling manpower and material resources, resulting in a certain degree of uncertainty in the input parameters of the modelling [76,77]. The evaluation results based on MAT.TRIGRS (V1.0) show that the overall prediction accuracy is around 0.7 (Figure S1), which indicate that the prediction accuracy is reliable. However, due to the subjectivity of the input parameters, there are still some errors between the overall evaluation results and the actual landslides (Figure 14) and some areas with less landsliding are predicted as high-susceptibility areas. Therefore, how to obtain accurate input parameters on a regional scale remains an important constraint for rainfall-induced landslide susceptibility assessment based on physically based models.

6. Conclusions

The objective of this study was to examine the landslides that occurred during the heavy rainfall event from 5 to 10 May 2016 in the Sanming area and to identify the geological, geomorphological and hydrometeorological factors that contributed to landslide hazards. The rainfall event resulted in around 2700 landslides covering a total area of 2.8 km², predominantly in Xiaqu town. We analyzed the landslide distribution pattern and its relationship with various factors. Our findings suggest that elevation, relief and topographic wetness index (TWI) were not significantly correlated with the landslide abundance index, while hillslope gradient, distance to a river and total rainfall played a significant role in the occurrence of landslides. The Sinian mica schist and quartz schist (Sn-s) lithological types were found to be the most susceptible to landslides, with more than 35% of landslides occurring in only 10% of the area. This indicates that landslides are more likely to occur in Sn-s strata during rainfall events. Additionally, the study showed that southeast- and east-facing hillslopes are more susceptible to collapse than northwest-north-oriented hillslopes due to the influence of the summer southeast monsoon. To further examine the susceptibility of the area to landslides, we used the MAT.TRIGRS (V1.0) tool for spatio-temporal susceptibility assessment. The results showed that unstable areas mainly appeared on both sides of the gullies as the rainfall event began. By 8 am on 7 May, the unstable area within the study area rapidly increased. Our numerical simulations indicate that the preceding rainfall events with low intensity (before 5 May) increased the soil water

content and the short duration of heavy rainfall on 8 May caused the rapid saturation of soil water content, thus leading to the occurrence of massive landslides in the Sanming area. Based on the findings, we recommend that more attention should be given to Sn-s lithological types in the region during the planning and implementation of landslide hazard mitigation measures. Additionally, our study highlights the importance of considering the influence of monsoons on landslide susceptibility in the area. Future studies could consider using high-resolution satellite images and other remote sensing techniques to monitor and map the landslide distribution in the study area, as well as to assess the effectiveness of the mitigation measures implemented.

Supplementary Materials: The following supporting information can be downloaded at: <https://www.mdpi.com/article/10.3390/rs15112738/s1>. Figure S1. Prediction curves of simulation results over different time periods; Table S1. Mechanical and hydrological parameters for different lithological types in landslide abundance areas. References [78–83] are cited in the Supplementary Materials.

Author Contributions: The research concept was proposed by C.X. who also contributed to the data curation and analysis. S.M. designed the research framework, processed the relevant data and drafted the manuscript. X.S. participated in the data analysis and contributed to the manuscript revisions. All authors have read and agreed to the published version of the manuscript.

Funding: This study was supported by the National Key Research and Development Program of China (2021YFB3901205).

Data Availability Statement: The source code of MAT.TRIGRS (V1.0) (<https://doi.org/10.1016/j.nhres.2021.11.001>, Ma et al., 2022 [56]) is available at <https://github.com/Masiyuanlandslides/MAT.TRIGRS-V1.0> (accessed on 10 May 2023).

Acknowledgments: We thank Google Earth for the free-to-access satellite images used in this study. We would like to thank three anonymous reviewers for their comments, which are very useful for improving the quality of the MS.

Conflicts of Interest: The authors declare that they have no known competing financial interest or personal relationship that could have appeared to influence the work reported in this paper.

References

- Salciarini, D.; Godt, J.W.; Savage, W.Z.; Conversini, P.; Baum, R.L.; Michael, J.A. Modeling regional initiation of rainfall-induced shallow landslides in the eastern Umbria Region of central Italy. *Landslides* **2006**, *3*, 181–194. [\[CrossRef\]](#)
- Montrasio, L.; Valentino, R.; Losi, G.L. Rainfall-induced shallow landslides: A model for the triggering mechanism of some case studies in Northern Italy. *Landslides* **2009**, *6*, 241–251. [\[CrossRef\]](#)
- Bordoni, M.; Vivaldi, V.; Lucchelli, L.; Ciabatta, L.; Brocca, L.; Galve, J.; Meisina, C. Development of a data-driven model for spatial and temporal shallow landslide probability of occurrence at catchment scale. *Landslides* **2020**, *18*, 1209–1229. [\[CrossRef\]](#)
- Bălteanu, D.; Chendeş, V.; Sima, M.; Enciu, P. A country-wide spatial assessment of landslide susceptibility in Romania. *Geomorphology* **2010**, *124*, 102–112. [\[CrossRef\]](#)
- Brunetti, M.; Peruccacci, S.; Rossi, M.; Luciani, S.; Valigi, D.; Guzzetti, F. Rainfall thresholds for the possible occurrence of landslides in Italy. *Nat. Hazards Earth Syst. Sci.* **2010**, *10*, 447–458. [\[CrossRef\]](#)
- Petley, D. Global patterns of loss of life from landslides. *Geology* **2012**, *40*, 927–930. [\[CrossRef\]](#)
- Wang, L.; Xiao, T.; Liu, S.; Zhang, W.; Yang, B.; Chen, L. Quantification of model uncertainty and variability for landslide displacement prediction based on Monte Carlo simulation. *Gondwana Res.* **2023**. [\[CrossRef\]](#)
- Ma, T.; Li, C.; Lu, Z.; Bao, Q. Rainfall intensity–duration thresholds for the initiation of landslides in Zhejiang Province, China. *Geomorphology* **2015**, *245*, 193–206. [\[CrossRef\]](#)
- Ma, S.; Shao, X.; Xu, C. Characterizing the Distribution Pattern and a Physically Based Susceptibility Assessment of Shallow Landslides Triggered by the 2019 Heavy Rainfall Event in Longchuan County, Guangdong Province, China. *Remote Sens.* **2022**, *14*, 4257. [\[CrossRef\]](#)
- Marc, O.; Gosset, M.; Saito, H.; Uchida, T.; Malet, J.-P. Spatial patterns of storm-Induced landslides and their relation to rainfall anomaly maps. *Geophys. Res. Lett.* **2019**, *46*, 11167–11177. [\[CrossRef\]](#)
- Broeckx, J.; Vanmaercke, M.; Duchateau, R.; Poesen, J. A data-based landslide susceptibility map of Africa. *Earth-Sci. Rev.* **2018**, *185*, 102–121. [\[CrossRef\]](#)
- Bălteanu, D.; Micu, M.; Jurchescu, M.; Malet, J.-P.; Sima, M.; Kucsicsa, G.; Dumitrică, C.; Petrea, D.; Mărgărint, M.C.; Bilaşco, Ş.; et al. National-scale landslide susceptibility map of Romania in a European methodological framework. *Geomorphology* **2020**, *371*, 107432. [\[CrossRef\]](#)

13. Dai, L.; Scaringi, G.; Fan, X.; Yunus, A.P.; Liu-Zeng, J.; Xu, Q.; Huang, R. Coseismic Debris Remains in the Orogen Despite a Decade of Enhanced Landsliding. *Geophys. Res. Lett.* **2021**, *48*, e2021GL095850. [CrossRef]
14. Xiong, J.; Chen, M.; Tang, C. Long-term changes in the landslide sediment supply capacity for debris flow occurrence in Wenchuan County, China. *Catena* **2021**, *203*, 105340. [CrossRef]
15. Kirschbaum, D.; Stanley, T. Satellite-based assessment of rainfall-triggered landslide hazard for situational awareness. *Earth's Future* **2018**, *6*, 505–523. [CrossRef]
16. Emberson, R.; Kirschbaum, D.; Amatya, P.M.; Tanyas, H.; Marc, O. Insights from the topographic characteristics of a large global catalog of rainfall-induced landslide event inventories. *Nat. Hazards Earth Syst. Sci.* **2022**, *22*, 1129–1149. [CrossRef]
17. Marc, O.; Stumpf, A.; Malet, J.P.; Gosset, M.; Uchida, T.; Chiang, S.-H. Initial insights from a global database of rainfall-induced landslide inventories: The weak influence of slope and strong influence of total storm rainfall. *Earth Surf. Dyn.* **2018**, *6*, 903–922. [CrossRef]
18. Chang, K.-t.; Chiang, S.-h.; Chen, Y.-C.; Mondini, A. Modeling the spatial occurrence of shallow landslides triggered by typhoons. *Geomorphology* **2014**, *208*, 137–148. [CrossRef]
19. Hirota, K.; Konagai, K.; Sassa, K.; Dang, K.; Yoshinaga, Y.; Wakita, E.K. Landslides triggered by the West Japan Heavy Rain of July 2018, and geological and geomorphological features of soaked mountain slopes. *Landslides* **2019**, *16*, 189–194. [CrossRef]
20. Bessette-Kirton, E.; Cerovski-Darriau, C.; Schulz, W.; Coe, J.; Kean, J.; Godt, J.; Thomas, M.; Hughes, K. Landslides triggered by Hurricane Maria: Assessment of an extreme event in Puerto Rico. *GSA Today* **2019**, *29*, 4–10. [CrossRef]
21. Van Westen, C.J.; Zhang, J. Landslides and Floods Triggered by Hurricane Maria (18 September 2017) in Dominica, Digital or Visual Products, UNITAR-UNOSAT. Available online: <https://www.unitar.org/unosat/node/44/2762> (accessed on 5 April 2023).
22. Saadatkhah, N.; Kassim, A.; Lee, L.M.; Rahnamarad, J. Spatiotemporal regional modeling of rainfall-induced slope failure in Hulu Kelang, Malaysia. *Environ. Earth Sci.* **2015**, *73*, 8425–8441. [CrossRef]
23. Chen, Y.-l.; Chen, D.-h.; Li, Z.-c.; Huang, J.-b. Preliminary studies on the dynamic prediction method of rainfall-triggered landslide. *J. Mt. Sci.* **2016**, *13*, 1735–1745. [CrossRef]
24. Merghadi, A.; Yunus, A.P.; Dou, J.; Whiteley, J.; ThaiPham, B.; Bui, D.T.; Avtar, R.; Abderrahmane, B. Machine learning methods for landslide susceptibility studies: A comparative overview of algorithm performance. *Earth-Sci. Rev.* **2020**, *207*, 103225. [CrossRef]
25. Guo, Z.; Torra, O.; Hürlimann, M.; Abancó, C.; Medina, V. FSLAM: A QGIS plugin for fast regional susceptibility assessment of rainfall-induced landslides. *Environ. Model. Softw.* **2022**, *150*, 105354. [CrossRef]
26. Melillo, M.; Brunetti, M.T.; Peruccacci, S.; Gariano, S.L.; Roccati, A.; Guzzetti, F. A tool for the automatic calculation of rainfall thresholds for landslide occurrence. *Environ. Model. Softw.* **2018**, *105*, 230–243. [CrossRef]
27. Guzzetti, F.; Gariano, S.L.; Peruccacci, S.; Brunetti, M.T.; Marchesini, I.; Rossi, M.; Melillo, M. Geographical landslide early warning systems. *Earth-Sci. Rev.* **2020**, *200*, 102973. [CrossRef]
28. Guzzetti, F.; Peruccacci, S.; Rossi, M.; Stark, C. Rainfall thresholds for the initiation of landslides in Central and Southern Europe. *Meteorol. Atmos. Phys.* **2007**, *98*, 239–267. [CrossRef]
29. Reichenbach, P.; Rossi, M.; Malamud, B.D.; Mihir, M.; Guzzetti, F. A review of statistically-based landslide susceptibility models. *Earth-Sci. Rev.* **2018**, *180*, 60–91. [CrossRef]
30. Baumann, V.; Bonadonna, C.; Cuomo, S.; Moscariello, M.; Biass, S.; Pistolesi, M.; Gattuso, A. Mapping the susceptibility of rain-triggered lahars at Vulcano island (Italy) combining field characterization, geotechnical analysis, and numerical modelling. *Nat. Hazards Earth Syst. Sci.* **2019**, *19*, 2421–2449. [CrossRef]
31. Tran, T.V.; Lee, G.; An, H.; Kim, M. Comparing the performance of TRIGRS and TiVaSS in spatial and temporal prediction of rainfall-induced shallow landslides. *Environ. Earth Sci.* **2017**, *76*, 315. [CrossRef]
32. Hong, Y.; Adler, R.; Huffman, G. Evaluation of the potential of NASA multi-satellite precipitation analysis in global landslide hazard assessment. *Geophys. Res. Lett.* **2006**, *332*. [CrossRef]
33. Nowicki Jessee, M.A.; Hamburger, M.W.; Allstadt, K.; Wald, D.J.; Robeson, S.M.; Tanyas, H.; Hearne, M.; Thompson, E.M. A global empirical model for near-real-time assessment of seismically induced landslides. *J. Geophys. Res. Earth Surf.* **2019**, *123*, 1835–1859. [CrossRef]
34. Fell, R.; Corominas, J.; Bonnard, C.; Cascini, L.; Leroi, E.; Savage, W. Guidelines for landslide susceptibility, hazard and risk zoning for land use planning. *Eng. Geol.* **2008**, *102*, 85–98. [CrossRef]
35. Sarkar, S.; Roy, A.K.; Raha, P. Deterministic approach for susceptibility assessment of shallow debris slide in the Darjeeling Himalayas, India. *Catena* **2016**, *142*, 36–46. [CrossRef]
36. Schiliro, L.; Montrasio, L.; Scarascia Mugnozza, G. Prediction of shallow landslide occurrence: Validation of a physically-based approach through a real case study. *Sci. Total Environ.* **2016**, *569–570*, 134–144. [CrossRef]
37. Montgomery, D.R.; Dietrich, W.E.; Torres, R.; Anderson, S.P.; Heffner, J.T.; Loague, K. Hydrologic response of a steep, unchanneled valley to natural and applied rainfall. *Water Resour. Res.* **1997**, *33*, 91–109. [CrossRef]
38. Pack, R.; Tarboton, D.; Goodwin, C.N. SINMAP 2.0—A Stability Index Approach to Terrain Stability Hazard Mapping, User's Manual. Produced in ArcView Avenue and C++ for Forest Renewal B.C. under Research Contract No: PA97537-0RE. Available online: https://digitalcommons.usu.edu/cee_facpub/16/ (accessed on 21 May 2023).
39. Montrasio, L.; Valentino, R.; Meisina, C. Soil saturation and stability analysis of a test site slope using the shallow landslide instability prediction (SLIP) model. *Geotech. Geol. Eng.* **2018**, *36*, 2331–2342. [CrossRef]

40. Zhang, K.; Xue, X.; Hong, Y.; Gourley, J.J.; Lu, N.; Wan, Z.; Hong, Z.; Wooten, R. iCRESTRIGRS: A coupled modeling system for cascading flood–landslide disaster forecasting. *Hydrol. Earth Syst. Sci.* **2016**, *20*, 5035–5048. [[CrossRef](#)]
41. Rossi, G.; Catani, F.; Leoni, L.; Segoni, S.; Tofani, V. HIRESSS: A physically based slope stability simulator for HPC applications. *Nat. Hazards Earth Syst. Sci.* **2013**, *13*, 151–166. [[CrossRef](#)]
42. Salvatici, T.; Tofani, V.; Rossi, G.; D’Ambrosio, M.; Tacconi Stefanelli, C.; Masi, E.B.; Rosi, A.; Pazzi, V.; Vannocci, P.; Petrolo, M.; et al. Application of a physically based model to forecast shallow landslides at a regional scale. *Nat. Hazards Earth Syst. Sci.* **2018**, *18*, 1919–1935. [[CrossRef](#)]
43. Baum, R.L.; Godt, J.W.; Savage, W.Z. Estimating the timing and location of shallow rainfall-induced landslides using a model for transient, unsaturated infiltration. *J. Geophys. Res. F Earth Surf.* **2010**, *115*. [[CrossRef](#)]
44. He, J.; Qiu, H.; Qu, F.; Hu, S.; Yang, D.; Shen, Y.; Zhang, Y.; Sun, H.; Cao, M. Prediction of spatiotemporal stability and rainfall threshold of shallow landslides using the TRIGRS and Scoops3D models. *Catena* **2021**, *197*, 104999. [[CrossRef](#)]
45. Lee, J.H.; Park, H.J. Assessment of shallow landslide susceptibility using the transient infiltration flow model and GIS-based probabilistic approach. *Landslides* **2015**, *13*, 885–903. [[CrossRef](#)]
46. Saadatkhah, N.; Kassim, A.; Lee, L.M. Hulu Kelang, Malaysia regional mapping of rainfall-induced landslides using TRIGRS model. *Arab. J. Geosci.* **2014**, *8*, 3183–3194. [[CrossRef](#)]
47. Sato, H.; Harp, E. Interpretation of earthquake-induced landslides triggered by the 12 May 2008, M7.9 Wenchuan earthquake in the Beichuan area, Sichuan Province, China using satellite imagery and Google Earth. *Landslides* **2009**, *6*, 153–159. [[CrossRef](#)]
48. Tian, Y.; Owen, L.A.; Xu, C.; Ma, S.; Li, K.; Xu, X.; Figueiredo, P.M.; Kang, W.; Guo, P.; Wang, S.; et al. Landslide development within 3 years after the 2015 Mw 7.8 Gorkha earthquake, Nepal. *Landslides* **2020**, *17*, 1251–1267. [[CrossRef](#)]
49. Gong, P.; Liu, H.; Zhang, M.; Li, C.; Wang, J.; Huang, H.; Clinton, N.; Ji, L.; Li, W.; Bai, Y.; et al. Stable classification with limited sample: Transferring a 30-m resolution sample set collected in 2015 to mapping 10-m resolution global land cover in 2017. *Sci. Bull.* **2019**, *64*, 370–373. [[CrossRef](#)]
50. Baum, R.L.; Savage, W.Z.; Godt, J.W. *TRIGRS—A Fortran Program for Transient Rainfall Infiltration and Grid-Based Regional Slope-Stability Analysis, Version 2.0*; US Geological Survey (USGS): Reston, VA, USA, 2008.
51. Alvioli, M.; Baum, R.L. Parallelization of the TRIGRS model for rainfall-induced landslides using the message passing interface. *Environ. Model. Softw.* **2016**, *81*, 122–135. [[CrossRef](#)]
52. Weidner, L.; Oommen, T.; Escobar-Wolf, R.; Sajinkumar, K.S.; Samuel, R.A. Regional-scale back-analysis using TRIGRS: An approach to advance landslide hazard modeling and prediction in sparse data regions. *Landslides* **2018**, *15*, 2343–2356. [[CrossRef](#)]
53. Tran, T.V.; Alvioli, M.; Lee, G.; An, H.U. Three-dimensional, time-dependent modeling of rainfall-induced landslides over a digital landscape: A case study. *Landslides* **2018**, *15*, 1071–1084. [[CrossRef](#)]
54. Iverson, R.M. Landslide triggering by rain infiltration. *Water Resour. Res.* **2000**, *36*, 1897–1910. [[CrossRef](#)]
55. Godt, J.; Baum, R.L.; Savage, W.Z.; Salciarini, D.; Schulz, W.; Harp, E.L. Transient deterministic shallow landslide modeling: Requirements for susceptibility and hazard assessments in a GIS framework. *Eng. Geol.* **2008**, *102*, 214–226. [[CrossRef](#)]
56. Ma, S.; Shao, X.; Xu, C.; He, X.; Zhang, P. MAT.TRIGRS (V1.0): A new open-source tool for predicting spatiotemporal distribution of rainfall-induced landslides. *Nat. Hazards Res.* **2021**, *1*, 161–170. [[CrossRef](#)]
57. Harp, E.; Michael, J.; Laprade, W. Shallow landslide hazard map of Seattle, Washington. *Rev. Eng. Geol.* **2008**, *20*, 67–82. [[CrossRef](#)]
58. Vieira, B.C.; Fernandes, N.F.; Augusto Filho, O.; Martins, T.D.; Montgomery, D.R. Assessing shallow landslide hazards using the TRIGRS and SHALSTAB models, Serra do Mar, Brazil. *Environ. Earth Sci.* **2018**, *77*, 260. [[CrossRef](#)]
59. Saulnier, G.-M.; Beven, K.; Obled, C. Including spatially variable soil depths in TOPMODEL. *J. Hydrol.* **1997**, *202*, 158–172. [[CrossRef](#)]
60. Bai, H.; Feng, W.; Yi, X.; Fang, H.; Wu, Y.; Deng, P.; Dai, H.; Hu, R. Group-occurring landslides and debris flows caused by the continuous heavy rainfall in June 2019 in Mibei Village, Longchuan County, Guangdong Province, China. *Nat. Hazards* **2021**, *108*, 3181–3201. [[CrossRef](#)]
61. Xu, Y. *Research on Evolution Process and Failure Mechanism of Pseudo-Soil Slope under Heavy Rainfall Action*; China University of Geosciences: Wuhan, China, 2014.
62. Zhao, Y. *Study on the Disaster Mechanism and Susceptibility Prediction Evaluation of the “7•9” Mass Debris Flow in Xiyan Village, Pucheng County, Fujian Province*; Chengdu University of Technology: Chengdu, China, 2021.
63. Ministry of Water Resources of the People’s Republic of China. *Standard for Engineering Classification of Rock Masses GB/T 50218-2014*; Standards Press of China: Beijing, China, 2014. [[CrossRef](#)]
64. Park, D.W.; Nikhil, N.V.; Lee, S.R. Landslide and debris flow susceptibility zonation using TRIGRS for the 2011 Seoul landslide event. *Nat. Hazards Earth Syst. Sci.* **2013**, *1*, 2547–2587. [[CrossRef](#)]
65. Qi, T.; Zhao, Y.; Meng, X.; Chen, G.; Dijkstra, T. AI-Based Susceptibility Analysis of Shallow Landslides Induced by Heavy Rainfall in Tianshui, China. *Remote Sens.* **2021**, *13*, 1819. [[CrossRef](#)]
66. Saito, H.; Korup, O.; Uchida, T.; Hayashi, S.; Oguchi, T. Rainfall conditions, typhoon frequency, and contemporary landslide erosion in Japan. *Geology* **2014**, *42*, 999–1002. [[CrossRef](#)]
67. Abancó, C.; Bennett, G.L.; Matthews, A.J.; Matera, M.A.M.; Tan, F.J. The role of geomorphology, rainfall and soil moisture in the occurrence of landslides triggered by 2018 Typhoon Mangkhut in the Philippines. *Nat. Hazards Earth Syst. Sci.* **2021**, *21*, 1531–1550. [[CrossRef](#)]

68. Marin, R.; García, E.; Aristizábal, E. Effect of basin morphometric parameters on physically-based rainfall thresholds for shallow landslides. *Eng. Geol.* **2020**, *278*, 105855. [[CrossRef](#)]
69. Yang, H.; Yang, T.; Zhang, S.; Zhao, F.; Hu, K.; Jiang, Y. Rainfall-induced landslides and debris flows in Mengdong Town, Yunnan Province, China. *Landslides* **2020**, *17*, 931–941. [[CrossRef](#)]
70. Hong, Y.; Hiura, H.; Shino, K.; Sassa, K.; Suemine, A.; Fukuoka, H.; Wang, G. The influence of intense rainfall on the activity of large-scale crystalline schist landslides in Shikoku Island, Japan. *Landslides* **2005**, *2*, 97–105. [[CrossRef](#)]
71. Hong, Y.; Hiura, H.; Shino, K.; Sassa, K.; Fukuoka, H. Quantitative assessment on the influence of heavy rainfall on the crystalline schist landslide by monitoring system -case study on Zentoku landslide, Japan. *Landslides* **2005**, *2*, 31–41. [[CrossRef](#)]
72. Martha, T.R.; Roy, P.; Govindharaj, K.B.; Kumar, K.V.; Diwakar, P.G.; Dadhwal, V.K. Landslides triggered by the June 2013 extreme rainfall event in parts of Uttarakhand state, India. *Landslides* **2015**, *12*, 135–146. [[CrossRef](#)]
73. Chen, Y.-C.; Chang, K.-t.; Wang, S.F.; Huang, J.-C.; Yu, C.-K.; Tu, J.-Y.; Chu, H.-J.; Liu, C.-C. Controls of preferential orientation of earthquake- and rainfall-triggered landslides in Taiwan's orogenic mountain belt. *Earth Surf. Process. Landf.* **2019**, *44*, 1661–1674. [[CrossRef](#)]
74. Rosso, R.; Rulli, M.C.; Vannucchi, G. A physically based model for the hydrologic control on shallow landsliding. *Water Resour. Res.* **2006**, *42*. [[CrossRef](#)]
75. Carrara, A.; Crosta, G.; Frattini, P. Comparing models of debris-flow susceptibility in the alpine environment. *Geomorphology* **2008**, *94*, 353–378. [[CrossRef](#)]
76. Westen, C.J. Landslide hazard and risk zonation-why is it still so difficult? *Bull. Eng. Geol. Environ.* **2005**, *64*, 5–23. [[CrossRef](#)]
77. Wu, S.-J.; Hsiao, Y.-H.; Yeh, K.-C.; Yang, S.-H. A probabilistic model for evaluating the reliability of rainfall thresholds for shallow landslides based on uncertainties in rainfall characteristics and soil properties. *Nat. Hazards* **2017**, *87*, 469–513. [[CrossRef](#)]
78. Smolíková, J.; Blahut, J.; Vilímek, V. Analysis of rainfall preceding debris flows on the Smědavská hora Mt., Jizerské hory Mts., Czech Republic. *Landslides* **2016**, *13*, 683–696. [[CrossRef](#)]
79. Yan, Y.; Hu, S.; Zhou, K.; Jin, W.; Ma, N.; Zeng, C. Hazard characteristics and causes of the “7.22” 2021 debris flow in Shenshuicao gully, Qilian Mountains, NW China. *Landslides* **2023**, *20*, 111–125. [[CrossRef](#)]
80. Chung, J.; Lee, Y.; Kim, J.; Jung, C.; Kim, S. Soil Moisture Content Estimation Based on Sentinel-1 SAR Imagery Using an Artificial Neural Network and Hydrological Components. *Remote Sens.* **2022**, *14*, 465. [[CrossRef](#)]
81. Kohler, M.A.; Linsley, R. *Predicting the Runoff from Storm Rainfall*; Research Paper No.34; Weather Bureau, US Department of Commerce: Washington, DC, USA, 1951.
82. Cantarino, I.; Carrion, M.A.; Goerlich, F.; Martinez Ibañez, V. A ROC analysis-based classification method for landslide susceptibility maps. *Landslides* **2018**, *16*, 265–282. [[CrossRef](#)]
83. Swets, J.A. Measuring the accuracy of diagnostic systems. *Science* **1988**, *240*, 1285–1293. [[CrossRef](#)] [[PubMed](#)]

Disclaimer/Publisher's Note: The statements, opinions and data contained in all publications are solely those of the individual author(s) and contributor(s) and not of MDPI and/or the editor(s). MDPI and/or the editor(s) disclaim responsibility for any injury to people or property resulting from any ideas, methods, instructions or products referred to in the content.